Journal of Industrial and Engineering Chemistry xxx (xxxx) xxx

Contents lists available at ScienceDirect

Journal of Industrial and Engineering Chemistry

journal homepage: www.elsevier.com/locate/jiec

Biofunctional properties and electrochemical behavior of loose sintering titanium alloys under simulated oral conditions and acidic dietary habits

Julio E. de la Rosa [a], Celia Garcia-Hernandez [b], Francisco J. García-García [b], Fernando Martín-Pedrosa [b], Yadir Torres [a], Cristina García-Cabezón [b,*]

[a] Departamento de Ingeniería y Ciencia de los Materiales y del Transporte, Escuela Politécnica Superior, Calle Virgen de África 7, 41011 Sevilla, Andalucía, Spain
[b] Departamento de Ciencia de Materiales e Ingeniería Metalúrgica, Escuela de Ingenierías Industriales, Universidad de Valladolid, Calle paseo del Cauce 59, 47011 Valladolid, Castilla y León, Spain

ARTICLE INFO

Keywords:
Porous implants
Loose sintering
Titanium alloys
Corrosion behavior
Coca-cola, artificial saliva

ABSTRACT

Commercially pure titanium (cpTi IV) and Ti6Al4V are widely used in dental implants due to their good mechanical properties and clinical reliability. However, their high elastic modulus may cause biomechanical mismatch with bone, and Ti6Al4V contains potentially cytotoxic elements such as Al and V. Additionally, exposure to acidic carbonated beverages may compromise implant longevity by accelerating corrosion. This study compares the biomechanical (stiffness and strength) and biofunctional (corrosion resistance and bioactivity) performance of cpTi IV and Ti6Al4V with a commercial Ti35Nb7Zr5Ta alloy, which features a lower elastic modulus and lacks cytotoxic elements. Although promising, Ti35Nb7Zr5Ta is more costly and requires more complex processing, warranting detailed evaluation. Disc-shaped samples were produced by loose sintering and fully dense processing to assess the influence of porosity. Corrosion behavior was analyzed using open circuit potential, electrochemical impedance spectroscopy, and potentiodynamic polarization in artificial saliva and Coca-Cola at 37 °C. Results show superior corrosion resistance for cpTi IV, balanced mechanical–corrosion behavior for Ti6Al4V, and improved biomechanical compatibility and bioactivity for Ti35Nb7Zr5Ta. Porosity and acidic conditions negatively affected passive film stability. These findings support optimization of titanium-based dental and orthopedic implants.

Introduction

Titanium and its alloys are the materials of choice for bone replacement, particularly in the field of dental implantology. Their extensive adoption is attributed to favorable characteristics, such as a high strength-to-weight ratio, good osseointegration, and acceptable corrosion resistance [1,2]. Since their initial use in implantology, cpTi IV and Ti6Al4V alloy have dominated the field, representing what is often called the first generation of biomedical titanium alloys [3,4].

However, the current research has highlighted important limitations associated with these materials. For instance, Ti6Al4V contains alloying elements that have raised concerns regarding long-term cytotoxicity and potential adverse biological responses [2,5,6]. Notably, vanadium has been associated with cytotoxic and carcinogenic effects, whereas aluminum has been implicated as a potential contributing factor in the development of Alzheimer's disease [5,7–9]. Furthermore, both cpTi and Ti6Al4V exhibit a relatively high elastic modulus (~100 GPa), which is significantly greater than that of natural bone, which typically ranges from 4 to 30 GPa depending on the bone type and measurement direction [3]. This mismatch can contribute to stress shielding effects, leading to bone resorption and eventual implant failure [5,10]. In response to these challenges, beta titanium (β-Ti) alloys, particularly those in the Ti-Nb-Zr-Ta (TNZT) group, have attracted increasing attention. Among them, Ti35Nb7Zr5Ta stands out because of its excellent biocompatibility [11], and promising mechanical properties for biomedical applications. TNZT alloys are composed of non-cytotoxic elements, effectively addressing and replacing the problems associated with vanadium and aluminum in traditional Ti6Al4V alloy. Furthermore, these alloys possess a lower elastic modulus, closer to that of human bone, which helps in the minimization of stress shielding problems [12], and promotes a more favorable load transfer to the surrounding tissue [13]. Although TNZT alloys typically involve higher production costs due to the price of the alloying elements added and the complexity of the manufacturing process, Ti35Nb7Zr5Ta is already

* Corresponding author.
E-mail address: crigar@uva.es (C. García-Cabezón).

https://doi.org/10.1016/j.jiec.2026.03.012
Received 25 January 2026; Received in revised form 3 March 2026; Accepted 15 March 2026
Available online 17 March 2026

commercially available and demonstrates a competitive profile compared to traditional titanium alloys.

On the other hand, the use of porous structures is an accepted approach to ensure mechanical requirements and reduce stress shielding of bone titanium implants. Porosity reduces the elastic modulus and allows physiological fluids to penetrate the implant, promoting the formation of new bone cells and tissue [14]. Technologies such us additive manufacturing [15,16], space holder techniques [17–20], and freeze casting [21–23] have been extensively investigated to find versatile, scalable, and easy-to-implement methods in the bone implant manufacturing industry. Different approaches exploring powder metallurgy routes offer an easy and cost-effective way to manufacture small titanium implants for bone replacement [24–27]. One of the main advantages of these methods is the ability to modify the porosity level, pore size, and distribution, allowing the fabrication of implants with a wide range of porosity and interconnected pores that favor bone ingrowth and osseointegration. However, the increased surface area and open porosity may also enhance corrosion susceptibility, potentially compromising long-term performance in the physiological environment [28,29].

Corrosion can lead to implant failure by compromising both its biocompatibility and its mechanical integrity [30]. Numerous in-vitro and in-vivo studies in humans and animals have reported cases of corrosion-induced deterioration, ion release, and inflammatory responses associated with titanium implants [31]. These corrosive processes are often triggered or accelerated by various physiological and mechanical conditions that compromise the stability of the protective surface layer. The passive oxide layer on titanium can be disrupted by mechanical loading, sliding contact, exposure to acidic environments, or a combination of these factors, leading to direct exposure of the underlying metal to the physiological medium and consequently enhancing its dissolution [31–33].

The underlying alloy composition and microstructure play a critical role in the electrochemical corrosion performance of the implant. Alloying elements influence the stability of the oxide film and its passivation behavior, directly affecting the interaction of the material with the surrounding biological environment [34]. The thin passive layer that forms on titanium alloys is essential, as it determines the corrosion mechanism and stability. This passive layer also significantly influences the biocompatibility, a key aspect of any biomaterial intended for implantation in the human body [35]. To understand the stability of passive films, several studies have investigated the behavior of titanium alloys in simulated physiological environments, correlating these findings with the corrosion resistance assessed by electrochemical techniques such as open circuit potential (OCP), electrochemical impedance spectroscopy (EIS), Mott-Schottky (MS) analysis, as well as potentiodynamic polarization (PDP) and CPDP.

Different simulated physiological media have been employed to evaluate the corrosion behavior of titanium alloys used in bone implantology, including Hank's solution [36–40], NaCl solutions [41–43], simulated body fluid (SBF) [44], phosphate-buffered saline (PBS) [35,45–47], artificial saliva [48–51], or Ringer's solution [52–54], among others. In these media, the passive film of commercially pure titanium is predominantly composed of TiO_2, which also forms the main protective layer in most titanium alloys. In TiAlV and TiAlNb ternary alloys, the passive film may additionally contain a relatively small amounts of titanium suboxides as well as Al2O3 and Nb_2O_5, which are generally located at the outer oxide-solution interface of the TiO2 matrix [35,39]. Meanwhile, beta titanium alloys such as TiNbZr and TNZT systems exhibit passive films enriched with Nb_2O_5 and ZrO_2 together with TiO_2, and also Ta_2O_5 in the case of TNZT, significantly improving the stability and corrosion resistance of the passive layer [44,47,52]. Samuel et al. [52] assessed the corrosion resistances of Ti35Nb7Zr5Ta, commercially pure titanium grade 2 and Ti6Al4V alloys in HCl solution as well as the corrosion resistances of TNZT and Ti6Al4V alloys in Ringer's solution. TNZT alloy exhibited superior corrosion resistance, maintaining a stable passive film without breakdown up to potentials above 5 V, whereas cpTi and Ti6Al4V showed film breakdown near 1.3 V and 1.5 V, respectively. In Ringer's solution, both TNZT and Ti6Al4V demonstrated high corrosion resistance without film breakdown, with similar corrosion potentials and no significant differences in passivation behavior. These findings highlight the influence of the titanium alloy composition and the nature of the physiological medium on the corrosion performance.

Regarding the testing medium, metalic biomaterials generally exhibit reduced passivation and increased corrosion rates in acidic environments, like those included in some dietary habits, compared to more neutral or slightly alkaline media. It is worth noting that the pH of carbonated beverages (~2.5) is markedly lower than that of saliva (~7.0) and well below the critical pH for enamel demineralization (~5.5) [55], representing one of the most aggressive acidic challenges encountered in the oral cavity. Coca-Cola exhibits a pH in the range of 2.44——2.74, placing it within a similar or even more acidic range than other common oral acidic agents such as lemon juice (pH ~ 2.7), vinegar (pH ~ 2.5), and sports drinks like Gatorade (pH ~ 3.78) [50,56–58]. Its corrosive potential, however, is not governed exclusively by acidity. The presence of phosphoric acid and the adhesion of carbon dioxide (CO_2) bubbles to metallic surfaces have been proposed as additional factors that may promote localized disruption of the titanium oxide passive film [56]. For example, Liu et al. [50] reported that exposure to Coca-Cola reduced the polarization resistance of titanium alloys by nearly 50%, accompanied by a decrease in passive film thickness from approximately 9.5 nm to 6 nm. This issue is especially relevant considering the extensive and frequent consumption of these beverage worldwide [57–59]. Approximately 45% of dental patients regularly consume carbonated beverages [59], with certain populations reaching an estimated intake of up to 12 cans per week [60]. Clinically, exposure to these beverages has been associated not only with enamel erosion but also with degradation of dental materials, potentially increasing the risk of cytotoxic effects due to metal ion release [56,58].

Although the clinical relevance of exposure to an acidic diet is recognized, only a limited number of studies have evaluated its impact on the corrosion of titanium alloys used in dental applications. Liu et al. [50] evaluated the passive film behavior of Ti0.3Mo0.8Ni (TA10) in a simulated oral environment containing Coca-Cola at different concentrations. The addition of Coca-Cola to the test solution decreases the corrosion resistance, as evidenced by an increase in the corrosion current density, a reduction in polarization resistance, and a thinning of the passive oxide layer. The lower pH and the presence of aggressive ions can compromise the integrity and inhibit the formation of the protective oxide film on titanium surfaces. In a similar study, Abalos et al. [60], after 28 days of immersion following a protocol simulating the daily consumption of a can of soft drink, concluded that soft drinks with low pH exert a corrosive effect on the surface of Ni-Ti orthodontic wires, and that the surface pattern plays a significant role in the severity of this process. In contrast, Faverani et al. [59] observed that neither cola soft drink nor artificial saliva produced significant changes in the surface topography or roughness (Ra) of cpTi and Ti6Al4V under repeated daily exposure conditions for 15 days. Additionally, Ti6Al4V demonstrated greater resistance to the tested solutions than cpTi.

Despite these contribution, comprehensive comparative studies evaluating porous α, α-β, and β titanium alloys under clinically relevant physiological and acidic conditions remain scarce. In particular, the corrosion behavior of these materials in both neutral environments, such as artificial saliva, and acidified media associated with common dietary habits, such as carbonated beverages, is still insufficiently explored. A systematic approach integrating alloy composition and microstructural porosity is therefore essential to assess their influence on passive film stability and corrosion kinetics under conditions that more closely mimic the complex oral environment.

This work systematically evaluates, for the first time, the relationship between alloy composition, porosity, and key functional properties of

three titanium-based materials widely used in bone implantology: cpTi IV, Ti6Al4V, and the low elastic modulus alloy Ti35Nb7Zr5Ta. From a clinical perspective, the material selection strategy aims to compare cpTi IV and Ti6Al4V, which remain widely used materials with well-established advantages and limitations, with a β-type alloy that has emerged as a promising alternative to address elastic modulus mismatch and biocompatibility concerns. The study focuses on the characterization of raw materials (commercial powders), and titanium alloy samples were fabricated using powder metallurgy. Two distinct strategies were used to explore the influence of porosity on material properties: loose sintering (LS), which represents the frontier of the porosity spectrum achievable with conventional powder metallurgy [12], and fully dense (FD) selected for comparative analysis. The LS process is highlighted as an economical and industrially scalable method to manufacture implants with porosity levels that improve mechanical compatibility with cortical bone, which offers significant potential impact on the bone implant market. The analysis comprises the composition and morphology, microstructural characteristics, porosity, micro-hardness, elastic modulus (via P-h curves), in vitro bioactivity (saturated-free plasma (SBF) immersion) and electrochemical corrosion behavior of the samples under simulated oral conditions and dietary habits (artificial saliva and Coca-Cola). This integrated approach provides valuable information on how to achieve the balance of mechanical integrity, corrosion resistance, and biological response required for advanced bone implant materials.

Materials and methods

To provide a comprehensive understanding of the biomechanical and biofunctional performances of the titanium-based materials under investigation, this study adopted a systematic experimental approach. This methodology involves sample fabrication using the limits of conventional powder metallurgy (LS), detailed characterization of porosity, microstructure, mechanical properties, electrochemical corrosion in simulated oral conditions and acidic dietary habits due to carbonated soft drinks consumption, and evaluation of in vitro bioactivity. Fully dense samples (FD) were prepared for comparative purposes. This allows the assessment of porosity on the studied properties. Fig. 1 summarizes the main stages of the methodology employed in this study, highlighting the key experimental techniques and parameters considered.

Samples fabrication by loose sintering: Limits of conventional powder metallurgy

In this study, three titanium alloys with extensive use and clinical relevance in bone implant applications were investigated: cpTi IV, Ti6Al4V, and Ti35Nb7Zr5Ta. These materials differ in mechanical properties, biocompatibility, and phases (α, α + β, and β, respectively), which influence their behavior in biomedical environments. The raw cpTi IV powder, grade 4 according to ASTM F67-13 [61], supplied by SENJONG Materials Co. Ltd. (Soul, Korea), were obtained by a hydrogenation/dehydrogenation process, resulting in particles with irregular morphology. In the case of alfa-beta alloy Ti6Al4V, grade 5 according to ASTM F136-13 [62], and beta alloy Ti35Nb7Zr5Ta, known commercially as TiOsteum® referenced in ASTM STP1471-EB [63], the powders provided by Ercata GmbH (Chemnitz, Germany) were obtained through atomization, resulting in spherical-shaped particles.

The particle size distribution of the powders used for each alloy was characterized based on d(10), d(50), and d(90) values, determined using a Mastersizer 2000 particle size analyzer (Malvern Panalytical Ltd., Malvern, UK). These values represent the particle diameters below which 10%, 50%, and 90% of the powder volume are found, respectively. As shown in Fig. 2, the cpTi IV IV powder exhibited the narrowest particle size distribution, Ti6Al4V had a broader distribution, and Ti35Nb7Zr5Ta displayed the widest distribution among the three alloys. These results indicate significant differences in powder granularity, which can influence densification behavior and microstructural evolution during sintering.

The powders were mixed in a Turbula Type T2C shaker mixer (TMG machines, Birmingham, UK) for 40 min as the first step in the manufacturing route for both LS and FD process. In the LS route, the powders were sintered without previous compaction. After mixing, they were directly deposited into an alumina cylinder with an inner diameter of 12 mm and later sintered in a Termolab furnace (Agueda, Portugal) under high vacuum conditions ($\sim 10^{-5}$ mbar). Sintering was performed at 1250 °C/2h for cpTi IV and Ti6Al4V, and at 1400 °C/2h for Ti35Nb7Zr5Ta. After that, each cylinder was sectioned to obtain three similar discs of approximately 5 mm of height.

To fabricate the FD discs, the powders were first vibrated in the steel mold with an inner diameter of 12 mm to achieve tap density. Subsequently, they were compacted by uniaxial and unidirectional pressing using a piston in an Instron Model 5505 universal testing machine, at a loading rate of 588 N/s and a dwell time of 2 min. The applied compaction pressure was determined for each alloy from its corresponding compressibility curve. A compaction pressure of 1300 MPa was used to obtain cpTi IV FD discs, whereas 1000 MPa was used for both Ti6Al4V and Ti35Nb7Zr5Ta titanium alloys. For each material, the amount of powder introduced into the mold was calculated based on the density and compressibility to obtain sintered discs with an approximate height of 5 mm in all cases. The sintering conditions were the same as those used for the LS samples of each corresponding material. Therefore, both compaction pressure and sintering temperature were adjusted for each alloy to achieve comparable densification and structural integrity. The differences between the discs obtained arise mainly from the intrinsic characteristics of the starting powders, which result in significantly different densification behaviors when identical processing parameters are applied.

Microstructural characterization of the sintered discs and corrosion studies were performed on samples with properly ground and polished surfaces; i.e. mirror-like finishing. Surface preparation started with sequential grinding using silicon carbide foil, from grit size 250 down to grit size 2500, to progressively remove surface irregularities. This was followed by a chemical–mechanical polishing step using a mixture of 90% colloidal silica and 10% hydrogen peroxide, which continued until a mirror-like surface finish was achieved, suitable for microstructural and surface analysis.

Porosity and microstructural characterization

Porosity measurements were performed by the Archimedes' method and image analysis. The latter, was carried out using an Olympus BX53M optical microscope, which was also used to observe the microstructural phases of each alloy. For the grain size measurements, the samples were chemically etched with Kroll's reagent for about 10 to 20 s, depending on the material, to reveal the grain boundaries. The grain size analysis was conducted following the ASTM E112 standard [64], specifically using the linear intercept method. Optical micrographs were acquired at 100x magnification, and the average grain size was calculated from ten representative images per sample from randomly selected regions across the surface, avoiding edges or anomalous areas. X-ray diffraction (XRD) analysis was performed to verify the crystalline structure and identify the phases present in each titanium alloy. The analysis was carried out using an Agilent Super Nova diffractometer (Agilent Technologies XRD Products, Yarnton, UK), equipped with micro CuKα/MoKα radiation and a CCD Atlas detector (Agilent Technologies XRD Products, OX5 1QU, Kidlington, UK).

Micro-mechanical behavior: Effect of porosity and chemical composition

The micro-mechanical behavior of the samples was experimentally assessed using a Microtest machine model MTR3/50–50/NI (Microtest

Fig. 1. Schematic representation of the titanium implant problems addressed in this work and the experimental methodology followed.

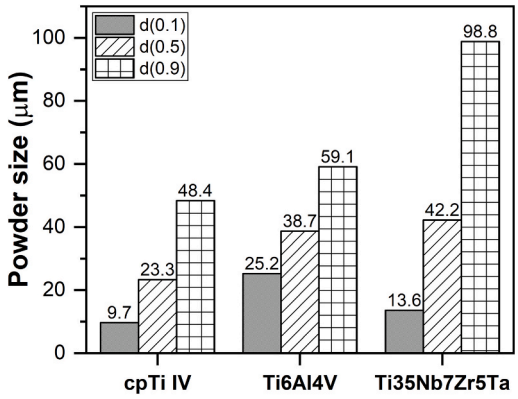

Fig. 2. Percentile particle size distribution for cpTi IV, Ti6Al4V, and Ti35Nb7Zr5Ta powders used in this work.

S.A., Madrid, Spain). Instrumented Micro-indentation tests were carried out under load control conditions, applying a maximum load of 2 N, with a loading rate of 2 N/min and a 15 s of dwell time. From the resulting load–displacement (P–h) curves, Young's modulus v (alues were calculated using the Oliver and Pharr analytical method [65,66], assuming a Poisson's ratio of 0.32 in all cases. Micro-hardness measurement were conducted using a micro-hardness tester Matsuzawa MXT70 equipped with a Vickers indenter, following the ASTM E384-22 standard [67]. All tests were performed with a maximum load of 300 gf and a dwell time of 10 s. For each sample assessed, at least 10 indentations were performed at randomly selected locations to ensure statistical reliability. Additionally, Young's modulus and yield strength were estimated based on porosity measurements using Nielsen's theoretical model [68] and the model proposed by Lascano et al. [18] respectively.

Electrochemical corrosion in artificial saliva and acidic carbonated beverages

To evaluate corrosion behavior under different physiological and aggressive conditions, two electrolytes were used: artificial saliva (pH ~ 5.5) and Coca-Cola (Coca-Cola Europacific Partners Iberia, S.L.U., Madrid, Spain). The inclusion of this widely consumed carbonated soft drink aimed to replicate a dietary scenario that could compromise the surface integrity of titanium implants. Coca-Cola is characterized for its low pH (~2.5) [50,56], as well as for containing carbonated water, sugar, colorant (E150d), phosphoric acid (acidulant), natural flavors, and caffeine taste. This makes Coca-Cola an appropriate medium for simulating an acidic dietary environment that can accelerate the degradation of metallic biomaterials. Coca-Cola was used as received, being freshly opened prior to each electrochemical test, to preserve its original carbonation. Both solutions were used at 37 ± 2 °C in a thermostated corrosion cell.

The electrochemical corrosion behavior of the samples was evaluated using a sequence of three standard tests. First, the open circuit potential (OCP) was monitored for 3600 s to assess the surface stabilization. Electrochemical impedance spectroscopy (EIS) measurements were then conducted three times per sample under OCP conditions to confirm system stability and evaluate the electrochemical properties of the passive film. The EIS data were acquired over a frequency range from 100 kHz to 10 mHz with an AC perturbation of 10 mV. Finally, cyclic potentiodynamic polarization (CPDP) test was performed to determine the corrosion potential (E_{corr}), corrosion current density (i_{corr}), and overall polarization behavior. The potential scan was conducted from −250 mV vs OCP to the reverse potential of 1500 mV vs Ag/AgCl, and then to the end potential of −100 mV vs Ag/AgCl, using a 50 mV/min scan rate. All electrochemical tests were repeated three times to ensure a good reproducibility.

The nominal geometric area of the surface exposed to the electrolyte was used to calculate the current densities and impedance values in all electrochemical measurements. Nevertheless, it is worth mentioning that the real electrochemically active area may be significantly larger due to their open porosity, particularly for the LS samples, affecting the absolute values of corrosion current density and impedance parameters when expressed per unit of geometric area.

To evaluate the corrosion performance and the influence of the testing media on each alloy, the polarization resistance (Rp) and corrosion rate (CR) were calculated. The polarization resistance was calculated using the Stern-Geary equation (Eq. (1)):

$$i_{corr} = \frac{1}{R_p} \bullet \frac{\beta_a \bullet \beta_c}{2.303 \bullet (\beta_a + \beta_c)} \quad (1)$$

where i_{corr} is the corrosion current density in A/cm^2, R_p is the polarization resistance in Ω/cm^2, β_a and β_c are the Tafel anodic and cathodic slopes respectively. Once the corrosion current density (i_{corr}) is determined experimentally, the corrosion rate, expressed in mm/year, can be estimated from the Faraday's law, using the following equation (Eq. (2)):

$$CR = \frac{K \bullet i_{corr} \bullet EW}{\rho} \quad (2)$$

where $K = 3.27 \cdot 10^{-3}$ mm·g/μA·cm·year is a unit conversion constant, EW is the equivalent weight of the alloy (g/equiv), and ρ is the material density (g/cm^3). This methodology has been described in detail in ASTM G102-89 [69].

For cpTi IV, the equivalent weight was calculated as the ratio between the atomic weight (W) and the valence number (n) of titanium using the following equation:

$$EW = \frac{W}{n} \quad (3)$$

For the titanium alloys, the equivalent weight was estimated based on the composition of all alloying elements using the following equation:

$$EW = \frac{1}{\sum \frac{n_i f_i}{W_i}} \quad (4)$$

where n_i is the valence of the ith element of the alloy, f_i is the mass fraction of the ith element in the alloy, and W_i is the atomic weight of the ith element in the alloy.

Immersion test in simulated body fluid

The ability of the samples to induce the formation of calcium phosphate was assessed by immersion in SBF for 4 weeks at 37 °C, following the guidelines established in ISO 23317-2014 [70]. SBF has an ion concentration similar to that of human blood plasma [71], and has been used to evaluate the ability of titanium alloys to induce the formation of phosphate-based layers on its surfaces. Upon completion of the incubation period, the samples were recovered, thoroughly rinsed with distilled water to remove loosely bound residues, and subsequently dried at room temperature. Surface analysis was conducted using a field emission scanning electron microscope (FE-SEM, FEI Teneo, Hillsboro, OR, USA). The elemental composition of the surface was examined by energy-dispersive X-ray spectroscopy (EDS) to identify calcium phosphate formation.

To complement the surface analysis, the SBF solutions after immersion were examined for calcium (Ca) and phosphorus (P) content using inductively coupled plasma optical emission spectroscopy (ICP-OES). Each solution was diluted with ultrapure water and subsequently acidified to a pH below 2.The Ca/P molar ratio was calculated to provide insights into the nature and stoichiometry of the phosphate deposits formed on the samples. In addition, an inductively coupled plasma mass

spectroscopy (ICP-MS) was employed to determine the concentration of metallic ions originating from the titanium alloys released into the SBF.

Results and discussion

Porosity, microstructure and grain size characterization of titanium alloys

The porosity results obtained through the Archimedes' method and image analysis demonstrate clear differences depending on both the manufacturing route and the alloy composition. As anticipated, the samples processed via the LS route exhibited significantly higher porosity compared to those fabricated by the FD route, due to the absence of a compaction step in LS that limits densification. Among the three titanium-based alloys analyzed, the β-type alloy Ti35Nb7Zr5Ta presented the highest porosity, followed by cpTi IV and Ti6Al4V. These findings are summarized in Fig. 3. To improve accuracy and minimize data noise during image analysis, pores with an area smaller than 10 μm2 were excluded from the quantification. The results are reported as total porosity (P_t) and interconnected porosity (P_i) from the Archimedes' method, and equivalent diameter (D_{eq}) and shape factor (F_f) from image analysis.

The porosity of LS samples was aproximately 22% for both cpTi IV and Ti6Al4V alloys, while the β-type Ti35Nb7Zr5Ta alloy exhibited the highest porosity (~30%). As expected, interconnected porosity (P_i) values were very close to the total porosity (P_t), indicating a high degree of pore interconnectivity. This characteristic can be advantageous for bioactivity and osseointegration because of the enhanced fluid permeability and biological interaction. In contrast, among FD samples, cpTi IV presented the lowest porosity (0.1–1.8%), whereas Ti6Al4V exhibited the highest porosity, reaching approximately 12% according to Archimedes' results. The Ti35Nb7Zr5Ta FD samples showed low porosity values, between approximately 1.3% (image analysis) and 3.2% (Archimedes' method), reflecting high densification. Regarding the morphology of the pores, D_{eq} values indicate that LS samples possess larger average pore sizes compared to FD samples across all alloys, with LS Ti6Al4V exhibiting the largest pores (~23 μm) and FD cpTi IV the smallest (~6 μm). F_f further reveals that pores in FD samples tend to be more regular and closer to circular shapes (~0.8–0.9), whereas LS samples exhibit more irregular pore morphologies with lower F_f values (~0.6). These pore morphologies are further illustrated in the optical micrographs presented below.

The observed variations in porosity have significant implications for material performance. Higher porosity in LS samples may contribute to reduced mechanical properties, as indicated by their lower hardness and stiffness values. However, increased porosity can also enhance bioactivity by promoting bone ingrowth, which is beneficial for osseointegration [12]. Nevertheless, porosity may compromise corrosion resistance, particularly in isolated pores, due to electrolyte trapping and oxygen exhaustion, increasing the surface vulnerability toward localized corrosion [72,73]. Therefore, the balance between porosity, mechanical integrity, and biofunctional properties must be carefully considered for biomedical applications.

Fig. 4 shows optical microscopy micrographs of the microstructures of the different titanium alloys obtained via the LS and FD routes. In the LS samples, the high porosity led to a severely deformed microstructure, complicating the precise measurement of grain size and hiding the distinction of grain boundaries. A similar observation was documented in a previous investigation conducted by some of the authors of this study [28]. In the FD samples, an equiaxed structure was observed for cpTi IV and Ti35Nb7Zr5Ta, while a Widmanstätten structure was observed for Ti6Al4V. The mean grain size of the FD samples was determined, and the results indicate that the Ti35Nb7Zr5Ta alloy exhibited the largest grain size (187.9 ± 40.7 μm), suggesting a coarser microstructure with higher variability. The cpTi IV presented an intermediate grain size (124.6 ± 34.2 μm), whereas the Ti6Al4V alloy displayed the smallest grains (79.5 ± 17.3 μm), indicating a finer and more homogeneous microstructure. The observed differences in grain size and microstructural features are directly related to the manufacturing routes employed. In the case of LS samples, the absence of external pressure and compaction during sintering results in limited grain boundary migration and densification, yielding high porosity, less defined grain boundaries, and severely unclear microstructures. In contrast, the FD samples experienced an additional compaction step and more effective densification, promoting enhanced grain boundary mobility and grain growth which result in clearer and well-defined microstructures.

These differences in grain size distribution may influence the mechanical properties of the titanium alloys, as finer grains are typically associated with increased strength [74]. Moreover, a finer grain structure can also affect the corrosion behavior by promoting progressive nucleation and growth of the passive film, resulting in a thicker, more compact, and less defective oxide layer on the surface [35,43,75].

XRD analysis was performed on FD samples of the three titanium alloys (Fig. 5). The diffraction patterns revealed distinct phase compositions that are consistent with the expected microstructures of each alloy. The cpTi IV sample exhibits characteristic peaks corresponding to the hexagonal close-packed (hcp) α-Ti phase. The Ti6Al4V alloy exhibited diffraction peaks associated with the α and β phases, which were consistent with its predominantly α + β microstructure. The TNZT alloy exhibits characteristic diffraction peaks of the body-centered cubic (bcc) β-Ti phase. Peaks correspond to the PDF® 05–0682 reference patterns for α-Ti phase and PDF® 44–1288 for β-Ti phase. These results demonstrate the successful phase formation expected from the alloy compositions.

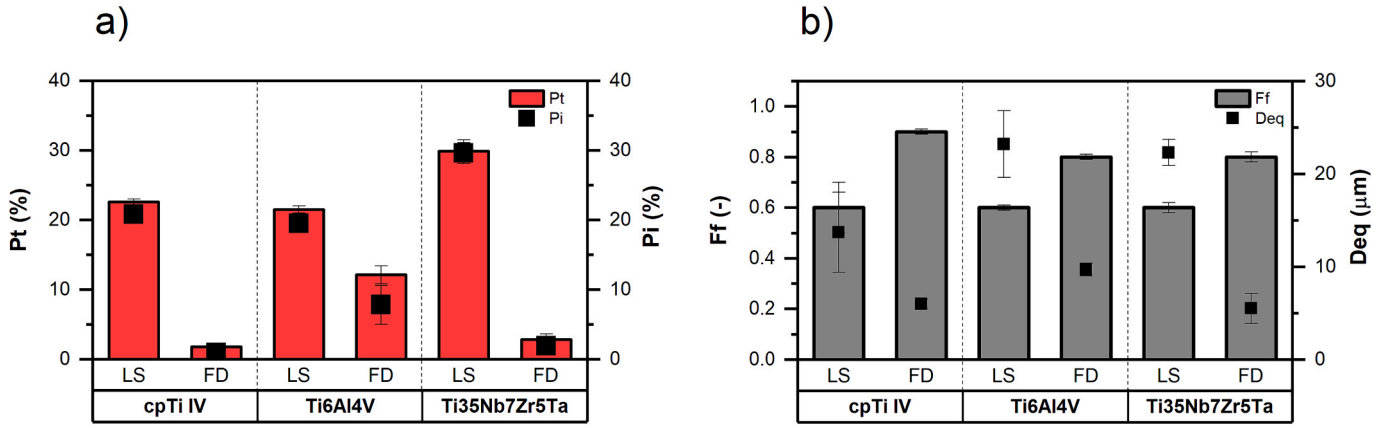

Fig. 3. (a) Total and interconnected porosity obtained by Archimedes' method, and (b) shape factor and equivalent diameter obtained by image analysis.

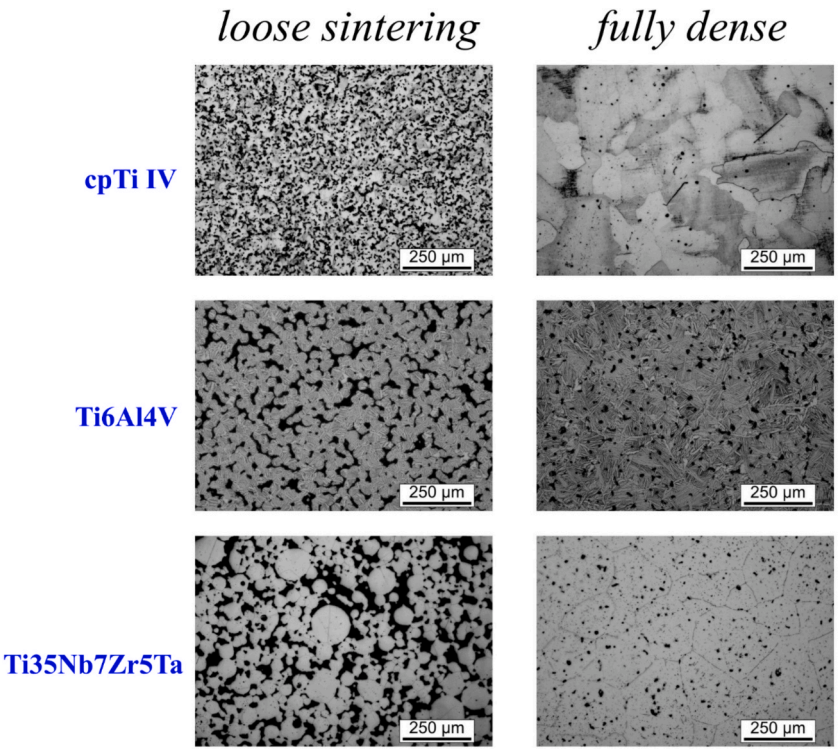

Fig. 4. Microstructure of LS and FD titanium alloy substrates revealed with Kroll's reagent.

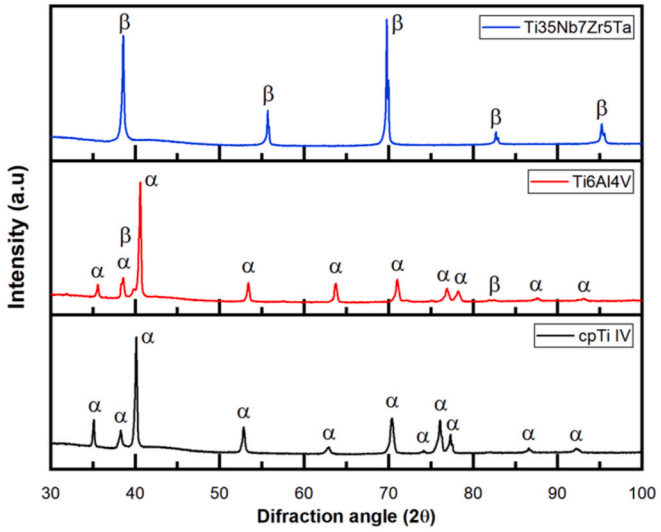

Fig. 5. XRD patterns of FD samples of Ti alloys, showing characteristic peaks corresponding to α-Ti and β-Ti phases indicated.

Mechanical characterization of titanium samples

The P-h curves in Fig. 6 illustrate the influence of alloy composition and processing route on the micromechanical behavior of the alloys. In the LS condition, Ti35Nb7Zr5Ta exhibits the highest penetration depth, indicative of a lower hardness and stiffness, likely related to its higher porosity and lower Young's modulus (see Supplementary Information Table S1). On the contrary, cpTi IV and Ti6Al4V display narrower penetrations and higher vertical loading slopes. For the FD curves, all alloys showed increased mechanical performances, with reduced penetration depths and increased slopes.

One of the main strengths of this study lies in the comparative approach conducted. While previous studies have independently examined the electrochemical and biofunctional performance of individual titanium-based alloys, few have directly compared cpTi IV, Ti6Al4V, and Ti35Nb7Zr5Ta under identical experimental conditions. This unified methodology ensures that the observed differences in performance can be reliably attributed to the intrinsic properties of the alloys and the effects of manufacturing routes, rather than variations in testing protocols. Furthermore, the inclusion of both fully dense (FD) and loose sintered (LS) samples provides insight into the role of porosity.

The impact of porosity is clearly reflected in the mechanical property measurements shown in Fig. 7. The elastic modulus values obtained experimentally for each alloy and processing route exhibit a strong correlation with those predicted by Nielsen's model, confirming the influence of porosity on the mechanical behavior. In parallel, the microhardness results (Fig. 7b) indicate that dense samples consistently exhibit higher hardness than their porous counterparts, further illustrating how porosity modulates mechanical strength. Although indentations were randomly performed to avoid visible surface pores, the presence of subsurface porosity in the vicinity of the indentation site may affect the measured hardness locally, leading to increased dispersion and occasional outliers.

Electrochemical corrosion in artificial saliva and Coca-Cola

Open circuit potential

The OCP measurements (Fig. 8) revealed that the alloy composition and degree of porosity clearly influenced the differences in electrochemical stability. From the recorded data, it was observed that initially exhibited a stabilization period, after which the potential tended to plateau, indicating the formation and consolidation of a passive oxide layer on the surface. From a thermodynamic perspective of the corrosion process, the studied titanium alloys exhibit a more noble state in Coca-Cola compared to artificial saliva. In most cases, the potential remained relatively stable, indicating the formation and maintenance of a passive layer on the analyzed surfaces. However, the OCP curve for LS cpTi IV in Coca-Cola shows slightly less regular behavior, which may indicate the presence of additional processes accompanying the passive film

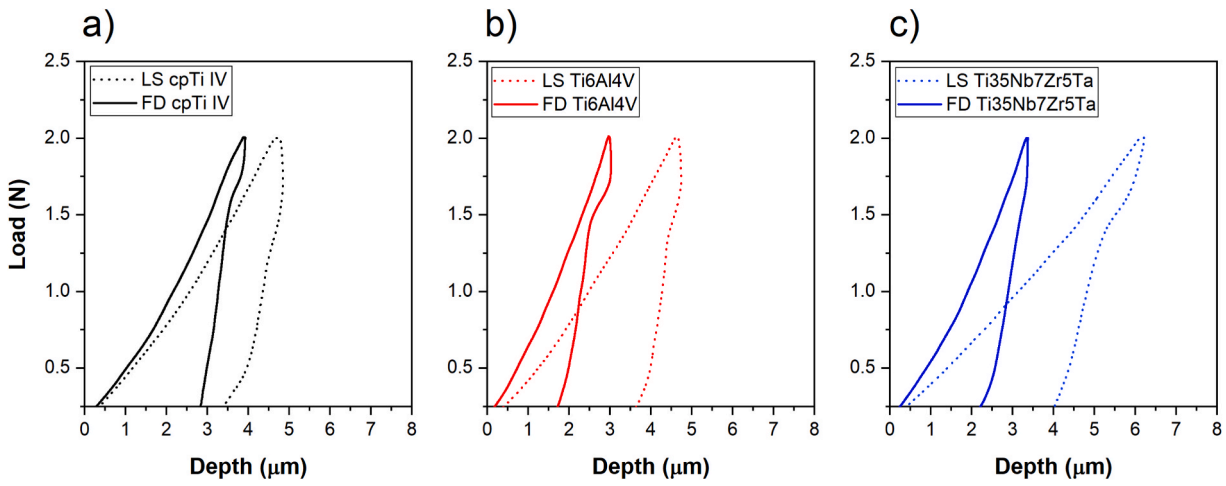

Fig. 6. P-h curves of LS and FD samples of Ti alloys.

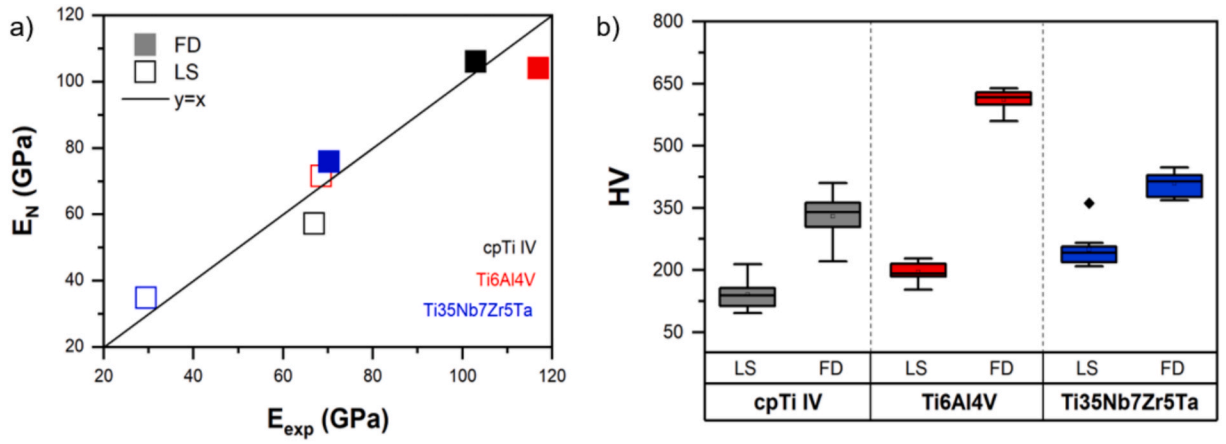

Fig. 7. (a) Comparison between the experimental elastic modulus (E_{exp}) and the values calculated by the Nielsen model (E_N) and (b) micro-hardness values.

formation. The TNZT alloy displays minimal potential variation across all conditions, suggesting the formation of a stable passive film; however, this material is slightly less noble than cpTi IV and Ti6Al4V.

The final OCP values are presented in Table 1 and serve as indicators of the thermodynamic tendency for corrosion. The results show that, in artificial saliva, cpTi IV exhibited the most positive potential among the LS samples, whereas Ti6Al4V displayed the highest potential among the FD samples. When Coca-Cola is used as the electrolyte, cpTi IV demonstrates the noblest behavior in both LS and FD conditions, although the differences are small compared to cpTi IV. These findings suggest that the nature of the electrolyte exerts a more significant influence on the thermodynamic corrosion behavior than the sample porosity. Notably, the OCP differences observed between LS and FD samples of the same material are relatively small (~15–25 mV) compared to the larger shifts observed for the same sample when tested in different media (~60–110 mV). Nevertheless, the FD samples exhibited more noble potential in all cases.

Electrochemical impedance spectroscopy

After OCP stabilization, EIS was performed to investigate the properties of the passive films formed on the tested materials. The impedance spectra provide valuable insights into the electrochemical processes occurring at the metal–electrolyte interface, reflecting the formation, structure, and protective behavior of the passive layer. Equivalent circuit (EC) models were established based on the physical and electrochemical characteristics of the passive films formed in artificial saliva and Coca-Cola, to analyze the impedance response and better understand the underlying corrosion resistance mechanisms. The experimental data and the corresponding simulated impedance spectra for the LS and FD samples of the titanium alloys are presented as Nyquist and Bode plots.

***Fig. 9 presents the Nyquist plots for the LS and FD samples in artificial saliva and Coca-Cola for cpTi IV (a-b), Ti6Al4V (c-d), and Ti35nb7Zr5Ta (e-f). All materials exhibited the typical characteristics of passive metallic surfaces. Among the samples, cpTi IV and Ti6Al4V show the largest arc diameter, especially in the FD condition, indicating superior corrosion resistance and a more stable passive layer. In contrast, the Ti35Nb7Zr5Ta alloy presents the smallest arc, suggesting a less protective passive film. Overall, the corrosion resistance was superior in artificial saliva, while the exposure to Coca-Cola significantly reduced the corrosion resistance, particularly for the FD samples of cpTi IV and Ti6Al4V.

In Fig. 10, the Bode plots for the impedance modulus (|Z|) reveal that |Z| increases markedly in the low-frequency range, with cpTi IV and Ti6Al4V maintaining the highest impedance values in both LS and FD. This behavior is consistent with the presence of a well-developed and stable passive film. On the contrary, Ti35Nb7Zr5Ta exhibits the lowest |Z| values among the three titanium alloys. At low frequencies, |Z| is similar for each sample in both artificial saliva and Coca-Cola; however, FD samples show higher impedance than LS in approximately one order of magnitude, highlighting how porosity reduces the material impedance.

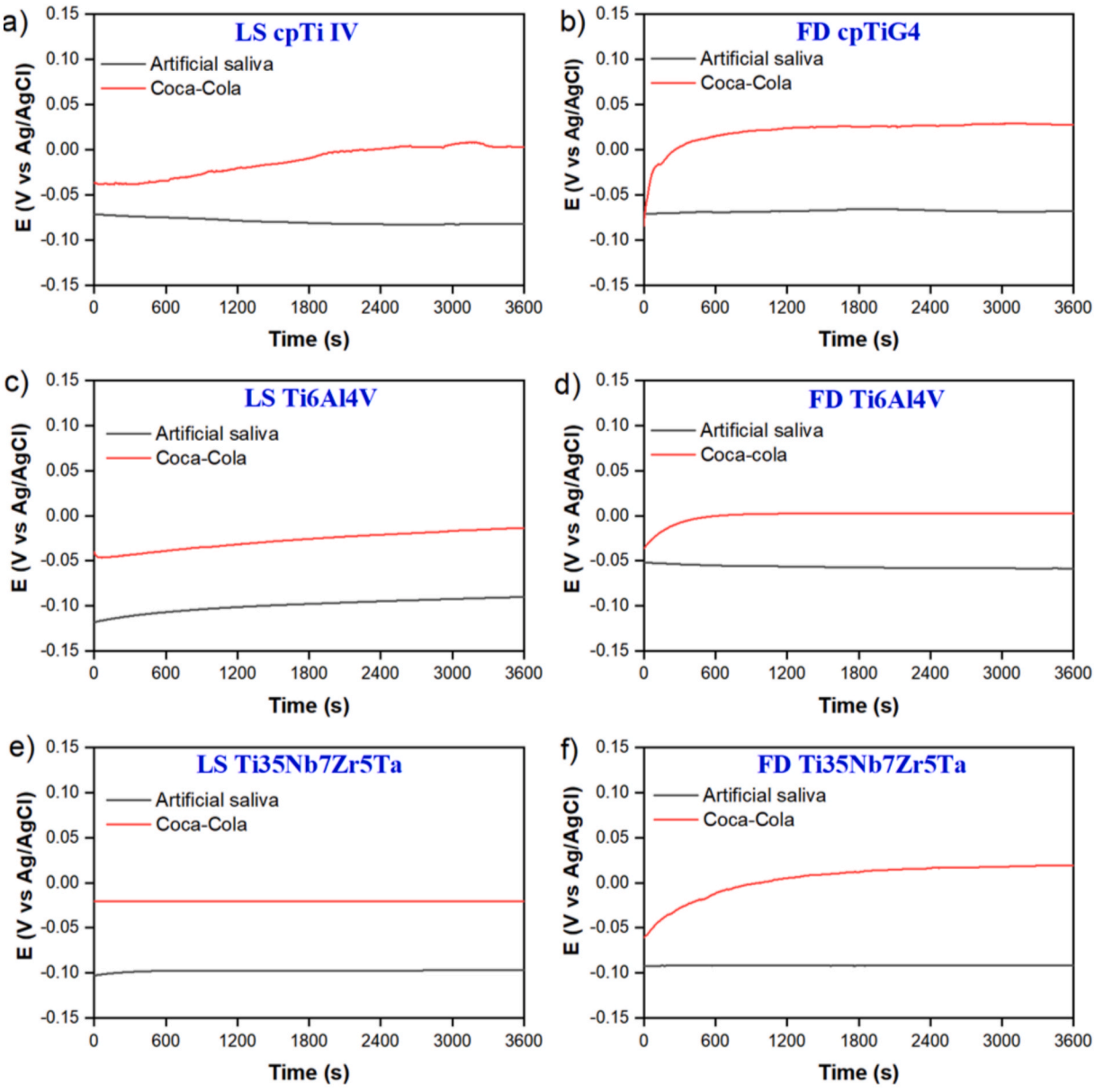

Fig. 8. OCP of Ti alloy samples measured in artificial saliva and Coca-Cola.

Table 1
Final OCP of titanium alloys in artificial saliva and coca-cola at 37 ± 2 °C.

Final OCP	cpTi IV		Ti6Al4V		Ti35Nb7Zr5Ta	
(mV vs Ag/AgCl)	LS	FD	LS	FD	LS	FD
Artificial saliva	−82	−68	−89	−58	−96	−91
Coca-Cola	3	27	−13	2	−21	19

This range of |Z| (10^4 to 10^6 Ω·cm^2) is consistent with previous findings reported in the literature for titanium-based materials tested in physiological environments. For instance, Liu et al. [50] reported |Z| around 10^5 Ω·cm^2 for Ti0.3Mo0.8Ni (TA10) immersed in three solutions at 37 °C: artificial saliva, Coca-Cola, and a mixture of both media. These results are in good agreement with those obtained in our study, particularly for FD samples, where slightly higher |Z| values were observed in artificial saliva compared to Coca-Cola. Similarly, Lario et al. [51] observed |Z| values in the order of 10^5 Ω·cm^2 for Ti35Nb7Zr5Ta tested in a fluorinated artificial saliva at 37 °C, using samples produced by powder metallurgy-based manufacturing routes. The tested samples exhibited residual porosity from 0.2 to 4.1%, with the denser samples exhibiting higher |Z| values. In the case of cpTi IV and Ti6Al4V, Mareci et al. [48] documented |Z| values around 10^6 Ω·cm^2 after 7 days of immersion in artificial saliva at 25 °C.

The Bode phase plots in Fig. 11 reveal no significant differences in the electrochemical processes of the FD samples in both media. All FD alloys exhibit a broad high phase angle plateau (−70° to −80°) at intermediate frequencies, indicating a well-developed passive oxide film. This response is typically associated with a bilayer passive structure, comprising a compact and highly protective barrier layer and an outer porous layer [38,51]. This suggests that the corrosion response in dense samples is dominated by capacitance and resistance, with minimal influence from solution or diffusion effects. In contrast, LS samples exhibit more complex behavior, especially for β-titanium alloy with a depressed phase angle and possibly diffusion-controlled process at low frequencies. This behavior could be explained by the higher surface area of the LS samples and the difficulty of the electrolyte fulfilling the porous structure and forming stable passive films.

Ta.

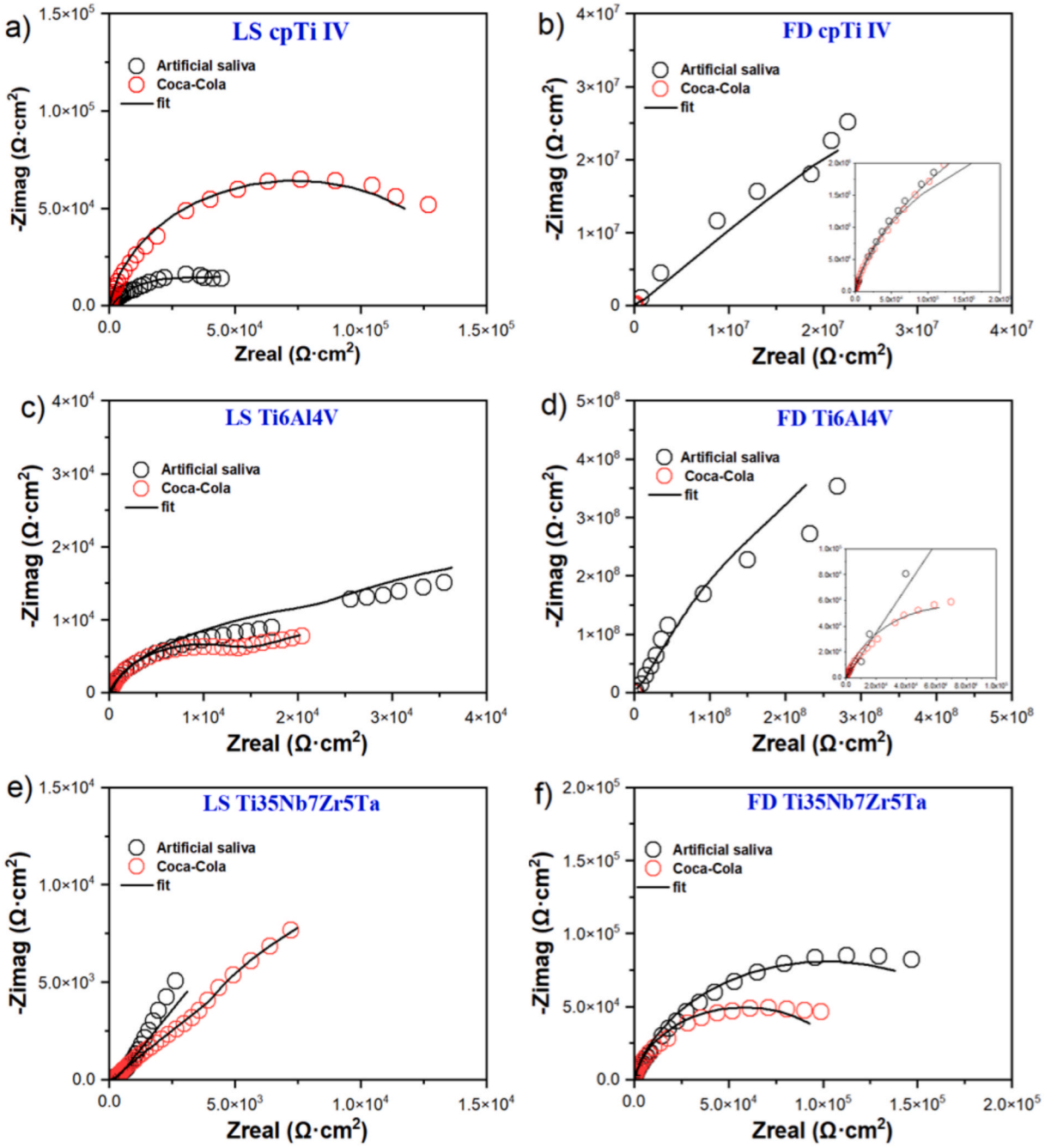

Fig. 9. Nyquist plots from EIS results of titanium alloys tested in artificial saliva and Coca-Cola.

The spontaneous formation of a stable passive film on titanium and titanium alloy surfaces typically manifests in two predominant morphological forms: a dense single-layer film [37,42,50,53,75,76] or a bilayer structure [38,39,43,44,47,51,77]. The single-layer passive film is usually compact, homogeneous, and very thin, on the order of a few nanometers (< 10 nm). Its high density provides excellent electrochemical stability and effective corrosion protection in a wide range of physiological environments. On the other hand, a two-layer passive film comprising a dense, compact inner barrier layer that serves as the main protective shield by preventing ion and electron transport, and a more porous outer layer. The outer porous layer generally exhibits lower impedance than the inner barrier layer.

***Fig. 12 shows the EC models used to fit the EIS data for the LS and FD samples. In both cases, the models represent a two-layer structure of the passive oxide film, comprising an outer porous layer in contact with the electrolyte and an inner compact barrier layer in contact with the titanium surface. This EC proposed in this study is the most commonly used for intepreting EIS data on titanium and its alloys exposed to physiological electrolytes [28]. This EC distinguishes three different frequency regions: The high frequency in the proposed circuit is related to the electrolyte resistance (R_S), and the responses at low and medium frequencies are related to the resistances of the inner barrier layer (R_{in}) and resistance of the porous outer layer (R_{out}) of TiO_2 respectively in the case of FD samples. In the case of LS samples, R_{out} corresponds to the electrolyte resistance inside the pores [28] and R_{in} to the resistance of the inner passive layer. Not only, the depression of the semicircle observed in the Nyquist plot and the phase shift (> −90°) observed in the Bode plots suggest the use of a constant phase element (CPE) instead of a pure capacitor. The impedance of a CPE is defined as:

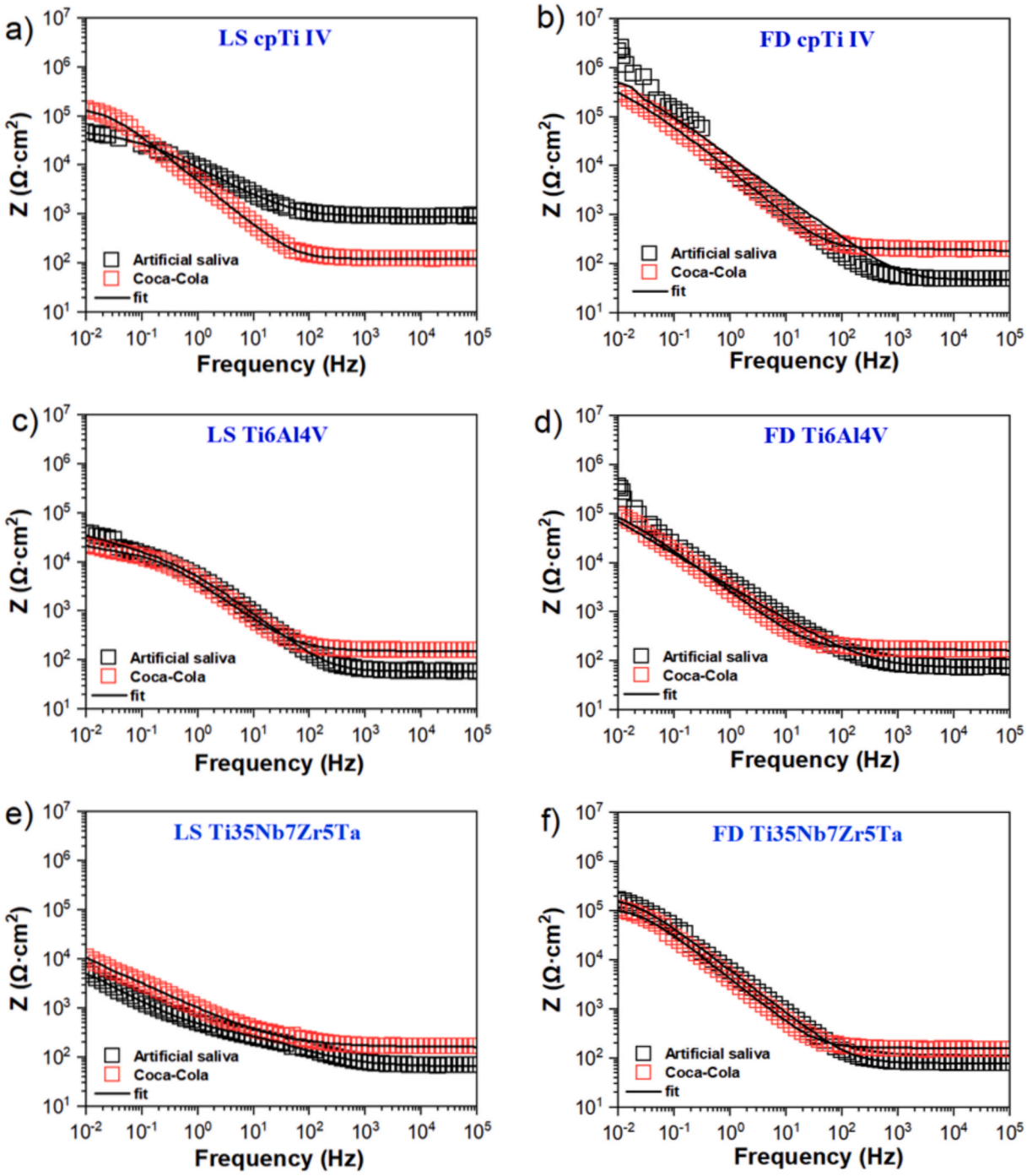

Fig. 10. Bode plots of impedance modulus from EIS results of titanium alloys tested in artificial saliva and Coca-Cola.

$$Z_{CPE} = \frac{1}{C(j\omega)^n} \quad (5)$$

where CPE for n = 1 corresponds to an ideal capacitor; for n = 0, CPE is an ideal resistance; and for n = -1 CPE t is a pure inductance. CPE_{out} corresponds to the outer surface capacitance and CPE_{in} to the inner layer capacitance respectively. In the case of the LS samples, the model needs the incorporation of an additional Warburg element (W) to describe the diffusion-controlled processes. Its inclusion here is likely related to ion diffusion within the interconnected porosity, where the passive film may be less stable or only partially developed. Previous EIS studies on titanium and titanium alloys in artificial saliva have demonstrated that the ionic transport through the passive TiO_2 film strongly influences the electrochemical response [78,79]. In porous titanium samples, the increased surface area, tortuosity, and electrolyte confinement within the pore network enhance mass transport limitations compared to dense materials. Consequently, diffusion-related phenomena may significantly contribute to the low-frequency impedance response. Therefore, a finite-length Warburg element was incorporated into the equivalent circuit to account for ionic transport within the porous structure and to achieve a physically meaningful fitting of the experimental data.

Table 2 summarizes the electrochemical parameters obtained from the fitting using the proposed EC models. A good accuracy of fit was achieved in all cases, with chi-square (χ^2) values in the order of 10^{-3}-10^{-4}. In each media, a significant decrease in both inner barrier layer resistance (R_{in}) and outer porous layer resistance (R_{out}) can be identified

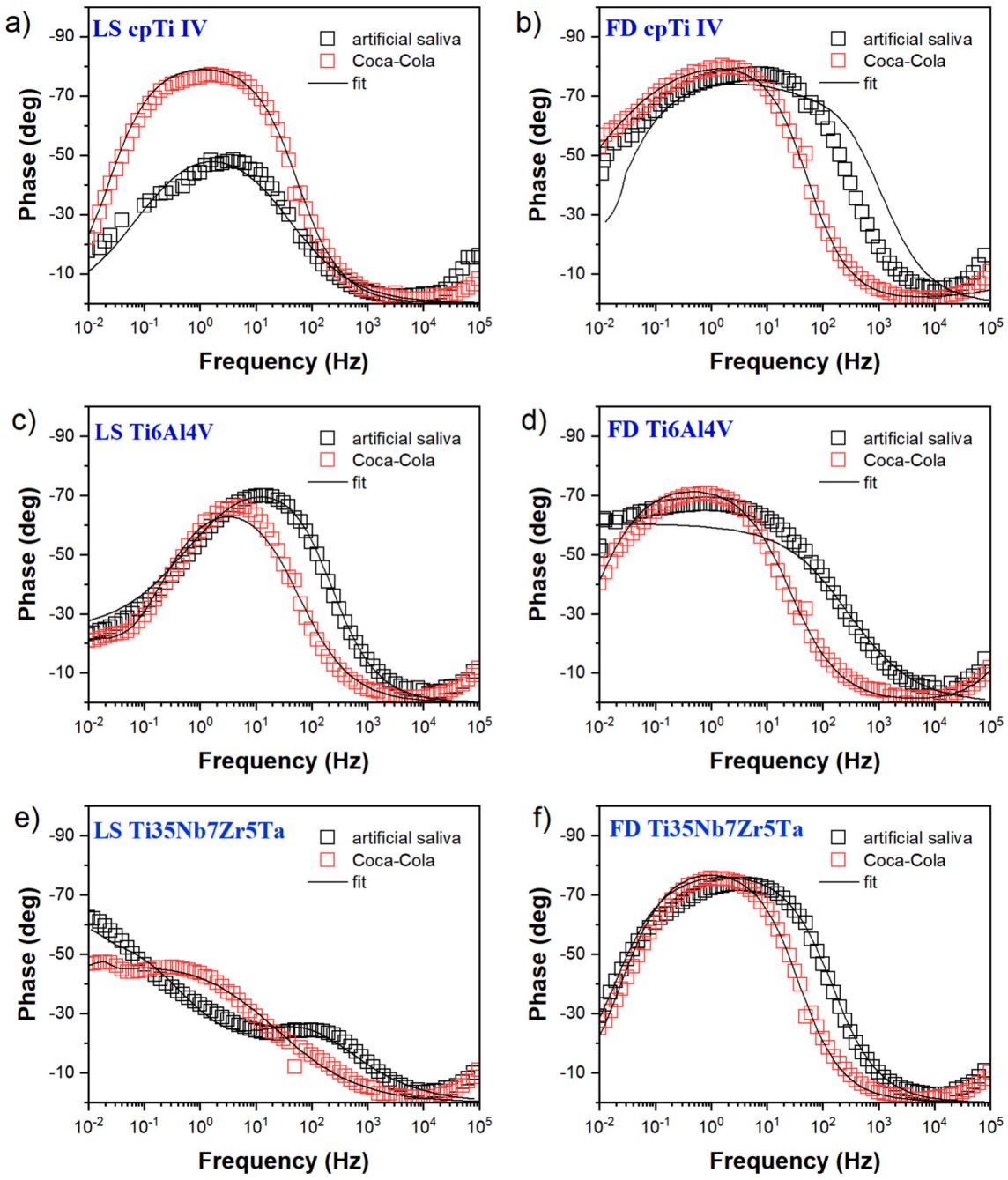

Fig. 11. Bode plots of phase angle from EIS results of titanium alloys tested in artificial saliva and Coca-Cola.

following the trend: cpTi IV > Ti6Al4V > Ti35Nb7Zr5Ta. In addition, the passive film resistances were generally higher in artificial saliva compared to Coca-Cola, highlighting the detrimental effect of the acidic environment on film stability.

The parameters obtained from the equivalent circuit fit showed that porosity is the most influential factor in electrochemical behavior. It was observed that for the three chemical compositions, the resistance to electron transfer ($R_{ct} = R_{out} + R_{in} + WR$) is clearly lower in the more porous samples, LS samples, which coincides with a lower impedance modulus at low frequency and higher double layer capacitance values. These results are consistent with the electrical impedance measurements performed on these three compositions [80,81]. In these studies, it was established that electrical impedance is directly related to porosity, with impedance values decreasing as the porosity of the samples increased.

Titanium and its alloys are widely used as implant materials due to their low density, excellent corrosion resistance, and high biocompatibility, largely attributed to the spontaneous formation of a stable passive titanium oxide layer in physiological environments. However, the introduction of porosity to titanium and titanium alloys, while beneficial for reducing elastic mismatch and enhancing bone ingrowth, significantly affects their electrochemical behavior in biological media. Several experimental studies have shown that increasing porosity generally leads to a decrease in corrosion resistance. For example, Makena and Shongwe reported that porous titanium foams fabricated by powder metallurgy exhibited a marked increase in corrosion current density and corrosion rate as porosity increased, likely due to larger electrolyte access and a less stable passive oxide film in porous structures [82]. Similarly, Fojt et al. investigated a Ti-39Nb alloy with varying porosity and observed that specimens with higher pore volume fractions demonstrated greater susceptibility to localized corrosion

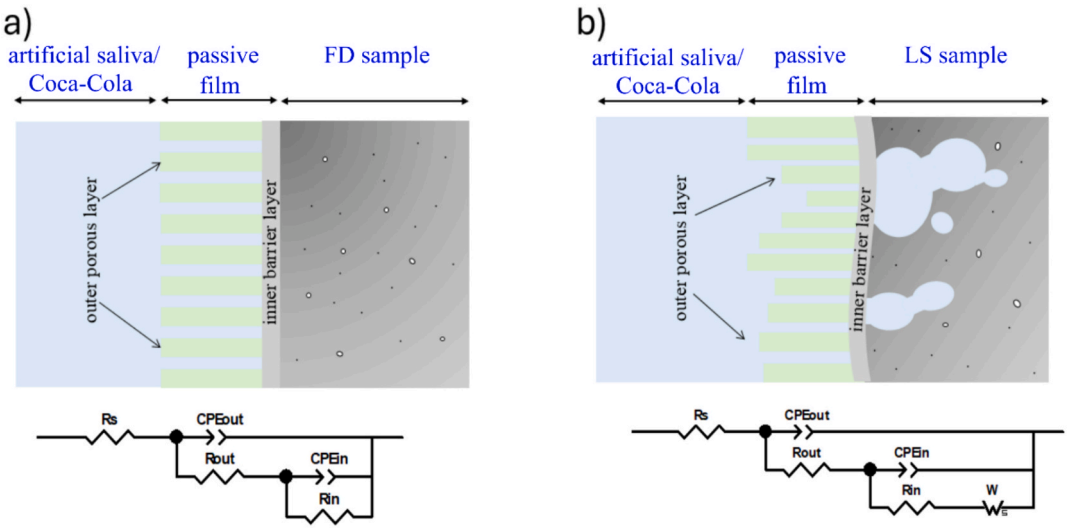

Fig. 12. Schematic representation of passive film formation and equivalent circuits for FD (a) and LS (b) titanium samples.

Table 2
Equivalent circuit parameters obtained from EIS of LS samples in artificial saliva and coca-cola at 37 ± 2 °C.

Sample	Electrolyte	R_S (kΩ/cm^2)	C_{out}-C (μF/cm^2)	C_{out}-n	R_{out} (kΩ/cm^2)	C_{in}-C (μF/cm^2)	C_{in}-n	R_{in} (kΩ/cm^2)	W-R (kΩ/cm^2)
LS cpTi IV	Artificial saliva	61.9	3.2	0.99	878.7	23.9	0.72	24.9	27.15
LS Ti6Al4V		59.5	28.2	0.99	170.0	33.6	0.79	12.2	28.05
LS Ti35Nb7Zr5Ta		77.7	25.0	0.88	67.6	14.9	0.75	3.2	13.67
LS cpTi IV	Coca-Cola	154.1	36.4	0.92	0.12	1.4	0.93	9.0	133.43
LS Ti6Al4V		159.4	22.1	0.95	0.13	2.2	0.80	13.8	45.80
LS Ti35Nb7Zr5Ta		166.6	50.0	0.91	0.01	2.7	0.89	0.2	29.08
FD cpTi IV	Artificial saliva	72.4	7.0	0.86	5.1	2	0.77	587.0	–
FD Ti6Al4V		73.1	60.2	0.84	3.8	1.4	0.83	502.5	–
FD Ti35Nb7Zr5Ta		79.0	32.8	0.87	1.4	8.2	0.81	195.6	–
FD cpTi IV	Coca-Cola	182.1	22.7	0.92	181.9	1.3	0.99	737.6	–
FD Ti6Al4V		170.2	7.8	0.89	0.7	0.5	0.98	145.0	–
FD Ti35Nb7Zr5Ta		160.6	41.5	0.88	0.02	4.5	0.98	117.2	–

attacks in simulated body solutions, particularly at porosities above 24%, where crevice corrosion became significant [83]. These findings are consistent with previous reports highlighting how pore morphology and connectivity can influence electrolyte penetration and destabilize the protective oxide layer [72].

The other important factor is the chemical composition. The three alloys showed high electronic transfer resistance values, although the beta-type alloys showed slightly lower values in both dense and porous samples. Similarly, the electrical impedance values were dependent on the chemical composition of the discs, and it was found that the microstructure had a decisive influence, revealing clear differences between the discs made with cpTi IV, Ti6Al4V, and Ti35Nb7Zr5Ta; the Ti6Al4V alloy was found to show the highest electrical impedance values for all frequencies in the case of completely dense samples [80]; this also coincides with better results for this composition in the EIS tests. The good correlation between the EIS and electrical impedance results indicates that both provide information on the state and thickness of the different titanium oxide layers and are therefore directly related to corrosion susceptibility.

Potentiodynamic polarization

The electrochemical corrosion kinetics of the alloys in artificial saliva and Coca-Cola, as illustrated by the CPDP curves in Fig. 13, reveal the combined effects of the processing route and alloy composition in each media. In artificial saliva, FD samples exhibit lower current densities throughout the passive region than their LS counterparts, indicating enhanced corrosion resistance likely due to reduced porosity and improved surface integrity. Results for Coca-Cola show that all samples display a broad passive region where the current density remains low and relatively constant as the potential is anodically swept. FD samples maintain significantly lower current densities throughout the passive range than their LS counterparts.

In LS samples, the actual surface area exposed to the test medium greatly exceeds the nominal geometric area, posing a methodological limitation for accurately determining current densities. In studies of corrosion behavior for both dense and porous metals, corrosion rates are commonly calculated from electrochemical measurements using the geometric surface area of the test specimen as the reference area because it provides a simple and reproducible basis for comparison. However, this approach inherently assumes that only the external projected area contributes to the electrochemical reactions, leading to systematic underestimation of the actual corrosion activity in highly porous samples.

The effective reactive surface area accessible to the corrosive medium in porous structures is significantly larger than the external geometric area due to internal pore surfaces, interconnectivity, and tortuous paths that permit electrolyte penetration deep within the material. Therefore, the true surface area where anodic dissolution and cathodic reduction can occur is much greater, and both the active area and the resulting corrosion rate are underestimated by normalization to the geometric surface area. This fact has been observed in other studies on foams and scaffolds [82,84]. So, in porous titanium foams, the corrosion current densities and derived corrosion rates increase by orders of magnitude with porosity (e.g., from ~ 10^{-9} to ~ 10^{-5} A · cm^{-2} when porosity increases from dense to ~ 70% Ti foam), reflecting the contribution of the interior surface area and less stable passive oxide films within pores that are not captured by the geometric area alone

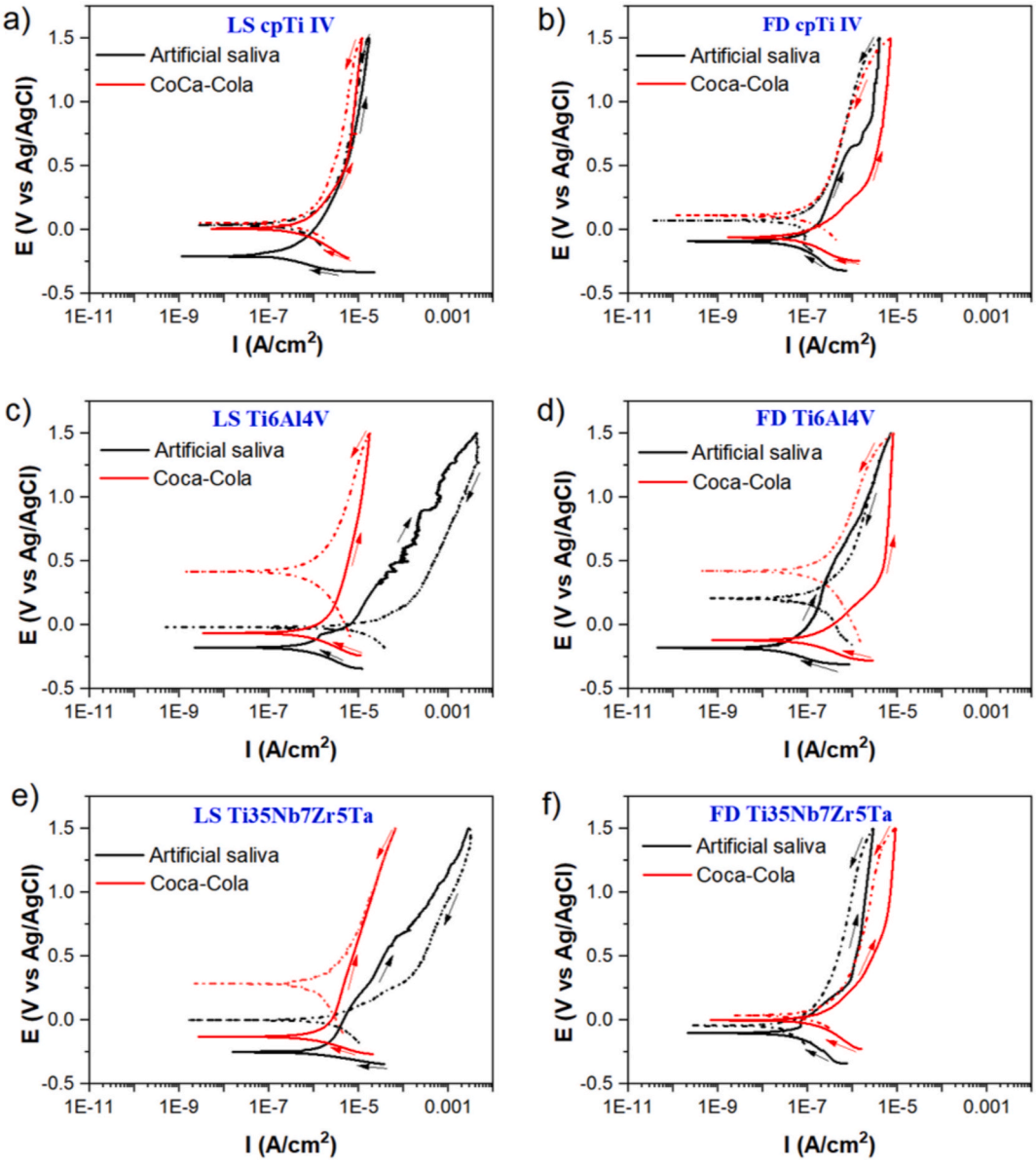

Fig. 13. CPDP curves of titanium alloys in artificial saliva and Coca-Cola.

[82].

Furthermore, it is well known that the morphology of pores, whether isolated or interconnected, plays an important role in the electrochemical behavior of porous materials. The electrolyte could be trapped in the case of isolated pores, resulting in crevice corrosion. On the contrary, the electrolyte could flow freely in interconnected pores, allowing oxygen substitution and the formation of passive layers [85].

The increased surface area of porous structures exposes more metal to corrosive environments. Detailed corrosion assessments on porous titanium fabricated via space-holder and spark plasma sintering also showed that samples with higher porosity exhibited elevated corrosion current densities and corrosion rates compared with dense counterparts, with the passive layer showing diminished stability inside pore networks [72,82]. This observation aligns with general electrochemical principles: increased roughness and high surface-to-volume ratio can enhance localized dissolution kinetics, particularly when oxygen transport into pores is limited. In contrast, some work on highly porous titanium scaffolds suggests nuanced behavior; Dabrowski et al. observed that although the corrosion resistance of porous titanium scaffolds (45–75% porosity) was lower than that of cast titanium, the most highly porous sample showed slightly improved corrosion parameters compared with intermediate porosity samples, potentially due to complex interactions of pore architecture and effective oxygen diffusion within interconnected pores [86]. These results underscore how the geometry, size distribution, and interconnectivity of pores can modulate the corrosion response beyond the simple porosity fraction alone.

In addition to the harmful impact of porosity on corrosion resistance, promoting localized corrosion phenomena within pores, there are other corrosion mechanisms that may become relevant depending on the microstructure of each alloy. For the Ti6Al4V alloy, characterized by a biphasic $\alpha + \beta$ microstructure, galvanic corrosion is expected to dominate, preferentially dissolving the α-phase over the β-phase. Conversely, in alloys with more homogeneous microstructures, such as commercially pure titanium or the predominantly β-phase Ti35Nb7Zr5Ta alloy, corrosion may preferentially occur at surface defects, such as microcracks, crevices, or grain boundaries, where oxygen penetration facilitates localized corrosion processes [42].

In artificial saliva, a positive hysteresis loop was observed in the LS samples of Ti6Al4V and Ti35Nb7Zr5Ta, whereas only Ti6Al4V exhibited a positive hysteresis loop among the FD samples, although with a

relatively small area. Albeit no breakdown potential was reached within the potential range studied, the presence of positive hysteresis suggests differences in the repassivation kinetics or surface oxide behavior between the samples, with the LS conditions potentially exhibiting slower or less efficient repassivation. In contrast, small areas of negative hysteresis were observed for the FD samples of cpTi IV and Ti35Nb7Zr5Ta, while LS cpTi IV sample showed almost identical current densities between up and down scan potentials within the passive region. Negative hysteresis typically indicates more efficient repassivation behavior, suggesting that these alloys, particularly LS samples for cpTi IV, and FD maintain a stable passive film with favorable electrochemical properties in artificial saliva. Negative hysteresis loops were obtained in all samples tested in Coca-Cola, with a notable decrease in current density observed in the following order: FD Ti6Al4V < FD cpTi IV < LS Ti6Al4V < FD Ti35Nb7Zr5Ta, indicating effective re-passivation behavior. On the other hand, the LS samples of cpTi IV and Ti35Nb7Zr5Ta exhibited minor hysteresis with nearly overlapping current densities in the passive region, indicative of highly stable passive films.

No signs of localized corrosion (pitting) were observed in either medium, which can be attributed to the test conditions and the applied potential range. These findings are consistent with those reported by Samuel et al. [52], who evaluated the anodic behavior of commercially pure titanium grade 2, Ti6Al4V, and Ti35Nb7Zr5Ta in HCl solution over a wide anodic potential range up to 5 V. Although the corrosion current density for the Ti35Nb7Zr5Ta alloy was higher than for cpTi IV and Ti6Al4V, its passive film proved to be more stable, as no breakdown potential was detected, whereas the other two alloys reached breakdown at around 3 V. When the authors later evaluated the performance in Ringer's solution for Ti6Al4V and Ti35Nb7Zr5Ta, no breakdown potential was observed for either alloy, suggesting the formation of a more stable passive film in this medium compared to the acidic environment.

Table 3 shows the E_{corr} and i_{corr} mean values obtained by Tafel analysis and R_p obtained by Stern-Geary equation. The material with the highest R_p in artificial saliva and Coca-Cola was cpTi IV, and corrosion resistance followed the order: cpTi IV > Ti6Al4V > Ti35Nb7Zr5Ta for LS and FD samples. The observed variations in corrosion resistance clearly depend on both the testing medium and the alloy composition. Superior performances are obtained in artificial saliva than in Coca-Cola. Ti6Al4V exhibited intermediate behavior, with susceptibility influenced by its alloying elements such as vanadium and aluminum. Additionally, all samples showed lower R_p values in Coca-Cola than in artificial saliva, clearly indicating reduced corrosion resistance in the acidic environment.

A third PDP test was performed using a 1:1 mixture of artificial saliva and Coca-Cola. This mixed medium is designed to simulate a more realistic oral environment where dietary habits cause intermittent exposure to both neutral and acidic conditions. The potential range for the potential scan corresponds to those previously evaluated in the CPDP tests performed separately in saliva and Coca-Cola, allowing a direct comparison of corrosion behavior. The primary objective of this test is to accurately determine the corrosion rate of the titanium-based alloys under these three conditions.

The corrosion rate of the titanium alloys, presented in Fig. 14, was calculated from PDP data to quantitatively assess their degradation behavior in different oral environments. As expected, the LS samples exhibited higher corrosion rates than their FD counterparts, which can be attributed to their greater surface area exposed to the environment, an effect that enhances the susceptibility of titanium alloys to corrosion [51]. The corrosion rate axis was plotted on a logarithmic scale to facilitate the comparison, allowing a clearer visualization of the trends among the three titanium-based materials for both LS and FD samples.

In all cases corrosion rate increased with the acidification of the testing medium following the addiction of Coca-Cola. This observation is consistent with the available literature, where several studies have shown that the corrosion rate of titanium alloys increases as the pH of the medium decreases. For instance, Braic et al. [87] investigated the corrosion behavior of Ti10Nb10Zr5Ta alloy in artificial saliva with pH values ranging from 2 to 7, reporting a significant increase in corrosion rate under acidic conditions, particularly at pH 2. Similarly, Vitelaru et al. [88] found that the corrosion rate of Ti6Al4V alloy in acidified artificial saliva (pH 2) was up to ten times higher than in neutral saliva (pH 5.2). In this study, when comparing the corrosion rates in artificial saliva with those obtained in more aggressive conditions, it is possible to observe significant increases, of up to three orders of magnitude. This demonstrates a substantial deterioration in the stability of the passive films on the alloy surfaces under acidic and complexing agent-rich conditions, which may better simulate realistic oral environments.

Regarding the chemical composition, Correa et al. [89] reported the same trend of the tested materials. The authors determined the corrosion rates of these alloys in modified Ringer-Harmann artificial saliva at 37 °C and obtained the following order in corrosion resistance based on the corrosion rate values: cpTi IV > Ti6Al4V > Ti35Nb7Zr5Ta.

Preliminary, drawing conclusions from immersion periods longer than the actual clinical exposure to carbonated beverages may appear to overestimate the corrosive challenge. In vivo, direct contact between dental materials and soft drinks is brief and intermittent. However, it has been documented that following the consumption of carbonated beverages, dental plaque pH may remain below the critical threshold (< 5.5) for more than 40 min and persist in an acidic range (< 6.2) for up to one hour [90], indicating that acidic conditions may extend well beyond the act of ingestion itself. Moreover, electrochemical characterization requires the system to reach a pseudo-steady-state condition to ensure reliable measurement of key corrosion parameters. Accurate determination of Rp, i_{corr}, E_{corr}, and passive film properties via EIS depends on prior stabilization of the OCP. Short or highly dynamic exposure protocols may not allow sufficient equilibration time, potentially affecting the reliability of passivation assessment and breakdown potential identification. Therefore, the use of continuous immersion under stable laboratory conditions should be interpreted as an informative approach, supporting the assessment of corrosion kinetics and passive film stability under these conditions.

Bioactivity evaluation in SBF

All the samples were immersed in SBF to evaluate the porosity and

Table 3
Electrochemical corrosion parameters in artificial saliva and Coca-Cola at 37 ± 2 °C obtained by Tafel analysis and Stern-Geary equation.

	cpTi IV		Ti6Al4V		Ti35Nb7Zr5Ta	
	LS	FD	LS	FD	LS	FD
Artificial saliva						
Ecorr (V vs Ag/AgCl)	−0.2	−0.1	−0.2	−0.2	−0.3	−0.1
icorr (μA/cm^2)	0.4	0.02	0.6	0.02	1.1	0.06
Rp (kΩ/cm^2)	125.3	1108.7	69.9	1026.5	46.4	971.3
Coca-Cola						
Ecorr (V vs Ag/AgCl)	0.01	−0.05	−0.1	−0.1	−0.1	−0.004
icorr (μA/cm^2)	0.9	0.1	0.7	0.1	1.8	0.3
Rp (kΩ/cm^2)	98.2	450.4	49.8	343.1	32.2	288.6

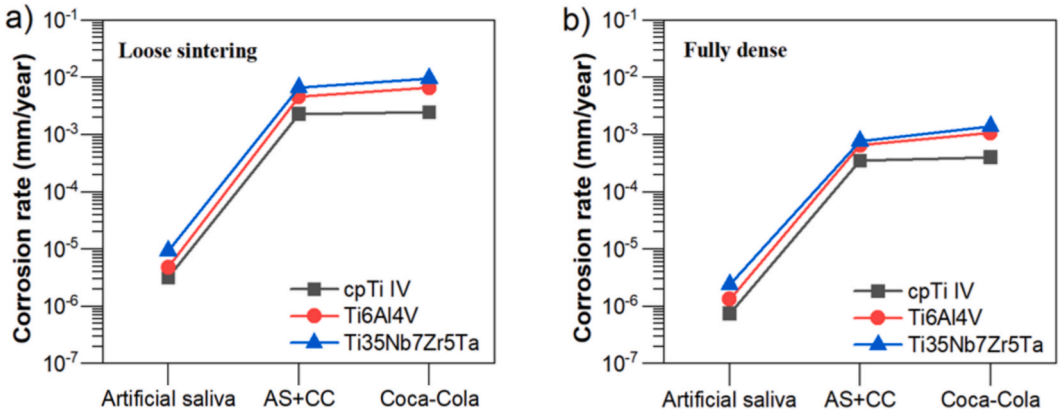

Fig. 14. Corrosion rate of titanium alloys in artificial saliva, Coca-Cola, and a 1:1 mixture of both solutions: Artifitial Saliva + Coca-Cola (AS + CC).

compositional elements influence on bioactivity. After four weeks of immersion, the samples were visually inspected using SEM to assess surface morphology changes associated with the formation of apatite and mineralized salts. Additionally, EDX was performed to identify the elemental composition of the formed layers. Significant differences in surface morphology between LS and FD samples are observed for each alloy in the SEM micrographs.

The cpTi IV IV LS sample (Fig. 15-a) exhibited a heterogeneous surface structure with dispersed mineral deposits, consistent with the initial apatite nucleation. The corresponding EDX spectrum confirms the presence of key elements such as oxygen (O), phosphorus (P), and sodium (Na). In contrast, their FD counterpart (see Supplementary Information Fig. S1a) shows a more continuous but non-uniform mineralized surface, characterized by agglomerated particles. The EDX spectrum of the FD sample revealed the presence of oxygen (O), phosphorus (P), calcium (Ca), sodium (Na), aluminum (Al), and chlorine (Cl), indicating the formation of calcium phosphate phases associated with apatite.

The Ti6Al4V LS sample (Fig. 15-b) exhibits a dense but heterogeneous surface morphology across the sample. The EDX spectrum reveals the presence of oxygen (O), phosphorus (P), calcium (Ca), chlorine (Cl), and magnesium (Mg), as well as alloy-specific elements such as titanium (Ti), aluminum (Al), and vanadium (V). In contrast, the Ti6Al4V FD sample (see Supplementary Information Fig. S1b) presents a more homogeneous, but smoother and thinner, mineralized layer over the surface. The EDX analysis of the FD sample detected oxygen (O), phosphorus (P), calcium (Ca), sodium (Na), chlorine (Cl), titanium (Ti), aluminum (Al), and vanadium (V), confirming the formation of a mineralized layer, although with a less developed morphology compared to the LS counterpart. Comparatively, the EDX spectrum of the LS sample shows more intense phosphorus (P) peaks and noticeably lower intensities of chlorine (Cl) and sodium (Na) peaks than the FD sample, indicating a higher degree of phosphate deposition.

A thin, heterogeneous and compact layer was observed on the Ti35Nb7Zr5Ta LS sample (Fig. 15-c). The corresponding EDX spectrum indicates the presence of oxygen (O), phosphorus (P), sodium (Na), silicon (Si), and titanium (Ti). In contrast, the Ti35Nb7Zr5Ta FD sample (see Supplementary Information Fig. S1c) exhibits a more complex surface morphology characterized by evident mineral deposits forming a homogeneous net-like structure. The EDX spectrum of the FD sample reveals oxygen (O), phosphorus (P), calcium (Ca), sodium (Na), silicon (Si), magnesium (Mg), chlorine (Cl), and titanium (Ti). For both LS and FD samples, silicon was detected in the EDX spectra of Ti35Nb7Zr5Ta samples, which has been associated with an active role in enhancing bioactivity [91,92], and its presence alongside phosphorus and sodium in both LS and FD samples suggests enhanced bioactivity and a greater potential for improved apatite formation.

The ICP-OES results presented in Table 4 show the concentrations of key ions (Ca, K, Mg, Na, and P) in the SBF after immersion of the LS and FD samples of the three titanium-based alloys, compared to the reference SBF solution. A general trend observed is the decrease in calcium and phosphorus concentrations relative to the reference, indicative of their consumption from the solution likely due to apatite nucleation and growth on the sample surfaces. Among the alloys, TNZT exhibits the greatest reduction in both Ca and P concentrations. The K, Mg, and Na concentrations remained relatively stable across all samples and the reference solution, reflecting their minor involvement in the mineralization process or equilibrium maintenance in the SBF.

The ICP-MS results presented in Table 5 indicate the concentrations of trace metallic ions released into the solution after sample immersion, relative to the reference medium. It is worth noting that ICP-MS detected trace amounts of elements not intentionally alloyed with some materials, such as Al in cpTi IV and TNZT, and Zr in cpTi IV. In the case of Al, a significant concentration was already present in the reference solution. These signals are attributed to background contributions, possible instrumental memory effects, or surface-related contamination rather than to actual alloy dissolution. Therefore, the results are interpreted comparatively, focusing on relative trends between alloys and processing routes rather than on absolute elemental concentrations. Notably, higher concentrations of metallic ions were detected in the LS samples, indicating that densification significantly reduces metal ion release, in agreement with the electrochemical corrosion results. Overall, the literature indicates a trade-off between porosity beneficial for mechanical and biological performance and corrosion resistance. Higher porosity tends to favor osseointegration and mechanical compliance closer to the bone, but it also generally increases the susceptibility to electrochemical attack in biological media due to enhanced electrolyte accessibility, reduced passive film stability, and the prevalence of local environments inside pores that can promote crevice corrosion.

Scientific evidence specifically focused on titanium and Ti6Al4V alloys demonstrates that substrate porosity strongly influences osteointegration by regulating bone ingrowth, vascularization, and mechanical interlocking at the bone–implant interface. Taniguchi et al. showed that additively manufactured porous titanium implants with approximately 65% porosity and an intermediate pore size achieved significantly greater bone ingrowth and mechanical fixation compared to smaller or larger pores [93]. Similarly, Ran et al. reported that 3D-printed porous Ti6Al4V scaffolds with pore sizes near 600 μm exhibited superior osteogenesis and in vivo osteointegration compared with 400 μm and 800 μm designs [94]. In addition, an in vitro and in vivo study demonstrated that Ti6Al4V scaffolds with interconnected pore sizes in the 400–700 μm range significantly enhanced cell proliferation, bone tissue penetration, and osseointegration compared with smaller pore architectures [95]. Collectively, these verified studies indicate that, in titanium and Ti6Al4V alloy implants, an interconnected porosity of approximately 60–70% with pore sizes close to 500–600 μm provides an optimal balance between biological performance and mechanical

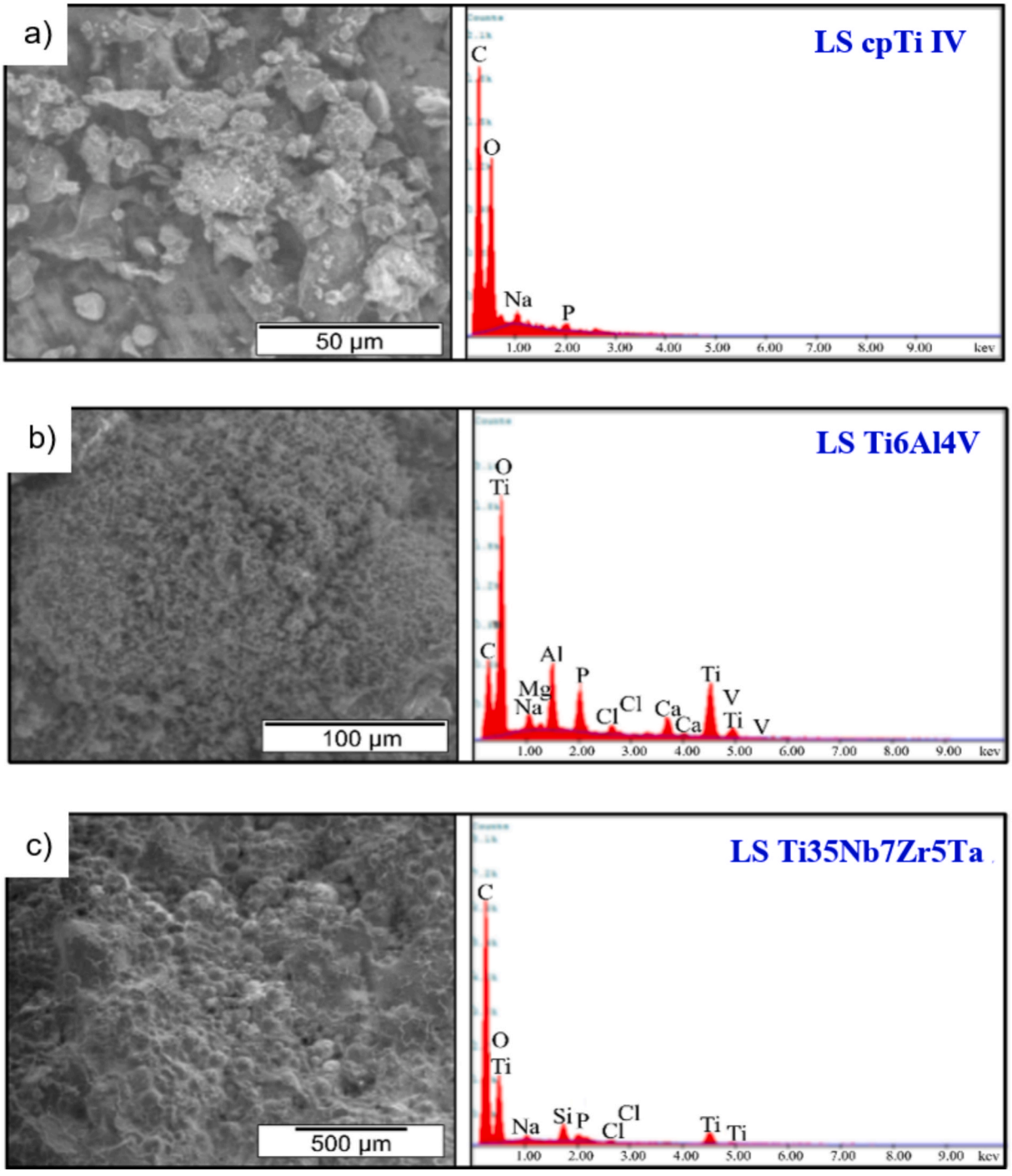

Fig. 15. SEM micrograph and EDX spectra of LS samples after 4 weeks of immersion in SBF at 37 °C.

Table 4
ICP-OES results for SBF elements.

Sample	Camg/l	Kmg/l	Mgmg/l	Namg/l	Pmg/l
Reference	115	200	37	3492	30.4
cpTi IV LS	107	212	37.8	3602	26.9
cpTi IV FD	98.5	209	37.8	3624	25.5
Ti6Al4V LS	108	209	37.5	3596	29.5
Ti6Al4V FD	106	210	37.8	3631	28.9
Ti35Nb7Zr5Ta LS	92	211	37.4	3601	28.7
Ti35Nb7Zr5Ta FD	91	208	36.9	3579	22.3

Table 5
ICP-MS results for titanium alloys elements.

Sample	Alµg/l	Nbµg/l	Taµg/l	Tiµg/l	Vµg/l	Zrµg/l
Reference	33.7	<0.25	<0.25	1.28	<0.25	<0.25
cpTi IV LS	29.9	<0.25	<0.25	116	<0.25	1.47
cpTi IV FD	22.3	<0.25	<0.25	5.41	0.32	<0.25
Ti6Al4V LS	118	<0.25<	<0.25	35.9	362	<0.25
Ti6Al4V FD	77.7	<0.25	<0.25	31.8	96.8	0.56
Ti35Nb7Zr5Ta LS	111	0.93	<0.25	5.67	0.49	1.04
Ti35Nb7Zr5Ta FD	12.7	0.29	<0.25	4.43	<0.25	<0.25

stability, thereby promoting robust and long-term osteointegration.

Among the alloys, TNZT consistently exhibited lower ion release

across all measured elements compared to the other materials, indicating superior chemical stability in SBF, whereas all its alloying elements were detectable in Ti6Al4V.

These ICP results and the SEM-EDX observations suggest that alloy composition and sample morphology influence the extent and quality of apatite layer formation. with Ti35Nb7Zr5Ta exhibiting particularly favorable bioactive mineral deposition.

Conclusion

The comprehensive analysis of the triad of essential properties for bone implant materials (mechanical performance-corrosion resistance-bioactivity) underscores the complex relationship between these key parameters and the influence of titanium alloy composition and porosity. Understanding how these factors interact is critical for optimizing the long-term success of bone implants. Based on the findings of this study. the following conclusions can be drawn regarding which structural configurations (dense or porous) and alloy compositions demonstrate the most favorable balance of properties for specific clinical requirements:

- Porosity was found to exert both beneficial and detrimental effects on the mechanical properties. depending on the evaluated parameters. Fully dense substrates exhibited higher hardness than the porous ones. whereas the elastic modulus of porous samples was significantly lower. reducing the risk of stress shielding. In terms of corrosion. porosity had a negative effect. reducing corrosion resistance in all tested environments compared to dense samples. primarily due to the greater surface area exposed to the electrolyte. EIS analysis also revealed lower passive film resistance in porous samples. with diffusion-controlled processes occurring at the electrolyte–metal interface inside pores. where the passive layer tends to be less stable. Similarly. the porous samples exhibited higher corrosion rates in all cases. It should be noted. however. that electrochemical parameters were calculated based on the nominal geometric area. and the larger effective surface area of LS samples may partially influence the quantitative comparison with fully dense substrates. However. SBF immersion tests demonstrated that. despite the higher metallic ion release observed in porous samples. they also showed greater surface mineralization and apatite formation. indicative of an enhanced bioactive response in all cases.
- Regarding alloy composition. the highest hardness values were recorded for Ti6Al4V and Ti35Nb7Zr5Ta. greater than those of cpTi IV. The TNZT alloy exhibited the highest hardness among the LS samples. while Ti6Al4V was the hardest among the FD samples. The lowest elastic modulus was obtained for Ti35Nb7Zr5Ta. especially under the LS condition. whose theoretical modulus was lower than the other alloys analyzed; with the addition of porosity. it reached values close to those of the cortical bone. The electrochemical corrosion behavior of the three materials was strongly affected by the acidification of the test medium. with corrosion rates increasing by up to three orders of magnitude when switching from artificial saliva to Coca-Cola. In all media tested. cpTi IV possessed the highest corrosion resistance. followed by Ti6Al4V. and Ti35Nb7Zr5Ta. However. the TNZT alloy showed the most promising bioactivity indicators in the SBF immersion tests.

These results indicate that porosity has a positive effect on bioactivity and reduces the risk of stress shielding but negatively affects corrosion behavior and mechanical strength. Furthermore. the chemical composition of the selected material has a significant impact on the overall properties. with TNZT alloys standing out as the most promising. not only due to their low elastic modulus. but also because they lack cytotoxic alloying elements. thus eliminating one of the main concerns associated with Ti6Al4V. However. there is still considerable room for improvement in the corrosion resistance of TNZT alloys. which. in the authors' opinion. could be addressed by surface modification strategies. Future work will focus on further characterizing these materials by evaluating their macrohardness. scratch resistance. dry wear performance. and tribocorrosion behavior under OCP and potentiostatic conditions.

CRediT authorship contribution statement

Julio E. de la Rosa: . **Celia García-Hernández:** Writing – review & editing, Writing – original draft, Methodology, Investigation, Conceptualization. **Francisco J. García-García:** Supervision, Project administration, Conceptualization. **Fernando Martín-Pedrosa:** Supervision, Software, Project administration, Conceptualization. **Yadir Torres:** Supervision, Project administration, Funding acquisition, Conceptualization. **Cristina García-Cabezón:** Writing – review & editing, Writing – original draft, Supervision, Project administration, Investigation, Funding acquisition, Data curation, Conceptualization.

Declaration of competing interest

The authors declare that they have no known competing financial interests or personal relationships that could have appeared to influence the work reported in this paper.

Acknowledgements

This work was supported by Junta de Castilla y Leon- FEDER VA117P24 and CLU-2019-04 BIOECOUVA Unit of Excellence and Ministerio de Ciencia Innovacion y Universidades -FEDER Plan Estatal (PID2021-122365OB-100). The author JER thanks to the Consejería de Transformación Económica. Industria. Conocimiento y Universidades de la Junta de Andalucía for supporting Project PREDOC PAID2020 (Ref. PREDOC_00680).

Appendix A. Supplementary data

Supplementary data to this article can be found online at https://doi.org/10.1016/j.jiec.2026.03.012.

References

[1] D.Q. Martins, W.R. Osório, M.E.P. Souza, R. Caram, A. Garcia, Electrochim. Acta 53 (6) (2008) 2809–2817, https://doi.org/10.1016/j.electacta.2007.10.060.
[2] M. Herbster, B. Garke, K. Harnisch, O. Michael, A. Lieb, U. Betke, M. Könnecke, A. Heyn, P. Kriegel, H. Thärichen, J. Bertrand, M. Krüger, T. Halle, J. Mech. Behav. Biomed. Mater. 164 (2025) 106899, https://doi.org/10.1016/j.jmbbm.2025.106899.
[3] M. Geetha, A.K. Singh, R. Asokamani, A.K. Gogia, Prog. Mater Sci. 54 (3) (2009) 397–425, https://doi.org/10.1016/j.pmatsci.2008.06.004.
[4] B.B. Straumal, N.Y. Anisimova, M.V. Kiselevskiy, K.M. Novruzov, A. Korneva, A. S. Gornakova, A.R. Kilmametov, S. Sommadossi, G. Davdian, Materials 16 (22) (2023) 7130, https://doi.org/10.3390/ma16227130.
[5] A. Sidambe, Materials 7 (12) (2014) 8168–8188, https://doi.org/10.3390/ma7128168.
[6] A.A. Elhadad, L. Romero-Resendiz, M.C. Rossi, L.M. Rodríguez-Albelo, S. Lascano, C.R.M. Afonso, A. Alcudia, V. Amigó, Y. Torres, J. Mater. Res. Technol. 33 (2024) 3550–3618, https://doi.org/10.1016/j.jmrt.2024.09.248.
[7] R.S. Bedi, D.E. Beving, L.P. Zanello, Y. Yan, Acta Biomater. 5 (8) (2009) 3265–3271, https://doi.org/10.1016/j.actbio.2009.04.019.
[8] K. Rokosz, T. Hryniewicz, S. Raaen, Int. J. Adv. Manuf. Technol. 85 (9–12) (2016) 2425–2437, https://doi.org/10.1007/s00170-015-8086-y.
[9] A. Azmat, M. Tufail, A.D. Chandio, Materials 14 (2021) 24, https://doi.org/10.3390/ma14247660.
[10] Z. Wally, W. Van Grunsven, F. Claeyssens, R. Goodall, G. Reilly, Metals (Basel) 5 (4) (2015) 1902–1920, https://doi.org/10.3390/met5041902.
[11] J. Cheng, P. Yang, Q. Chen, X. Long, G. Chen, J. Xu, W. Gui, T. Wu, J. Hu, J. Mater. Res. Technol. 32 (2024) 2268–2278, https://doi.org/10.1016/j.jmrt.2024.08.083.
[12] L.M. Rodriguez-Albelo, P. Navarro, F.J. Gotor, J.E. de la Rosa, D. Mena, F.J. García-García, A.M. Beltrán, A. Alcudia, Y. Torres, J. Mater. Res. Technol. 24 (2023) 6212–6226, https://doi.org/10.1016/j.jmrt.2023.04.212.
[13] A. Robau-Porrua, J.E. González, J. Rodríguez-Guerra, P. González-Mederos, P. Navarro, J.E. de la Rosa, M. Carbonell-González, E. Araneda-Hernández,

Y. Torres, J. Mater. Res. Technol. 29 (2024) 3255–3267, https://doi.org/10.1016/j.jmrt.2024.02.091.
[14] J. Gupta, S. Ghosh, S. Aravindan, Mater. Sci. Eng. C 123 (2021) 111962, https://doi.org/10.1016/j.msec.2021.111962.
[15] S. Tunchel, A. Blay, R. Kolerman, E. Mijiritsky, J.A. Shibli, Int. J. Dent. 2016 (2016) 1–9, https://doi.org/10.1155/2016/8590971.
[16] B. Ren, Y. Wan, C. Liu, H. Wang, M. Yu, X. Zhang, Y. Huang, Mater. Sci. Eng. C 118 (2021) 111505, https://doi.org/10.1016/j.msec.2020.111505.
[17] Y. Torres, S. Lascano, J. Bris, J. Pavón, J.A. Rodriguez, Mater. Sci. Eng. C 37 (1) (2014) 148–155, https://doi.org/10.1016/j.msec.2013.11.036.
[18] S. Lascano, C. Arévalo, I. Montealegre-Melendez, S. Muñoz, J.A. Rodriguez-Ortiz, P. Trueba, Y. Torres, Appl. Sci. 9 (5) (2019) 982, https://doi.org/10.3390/app9050982.
[19] S. Sahmani, M. Shahali, A. Khandan, S. Saber-Samandari, M.M. Aghdam, Appl. Clay Sci. 165 (2018) 112–123, https://doi.org/10.1016/j.clay.2018.08.013.
[20] Y. Torres, J.J. Pavón, J.A. Rodríguez, J. Mater. Process. Technol. 212 (5) (2012) 1061–1069, https://doi.org/10.1016/j.jmatprotec.2011.12.015.
[21] L. Zhang, R. Le Coz-Botrel, C. Beddoes, T. Sjöström, B. Su, Biomed. Mater. 12 (1) (2017) 015014, https://doi.org/10.1088/1748-605X/aa50a1.
[22] H.-D. Jung, S.-W. Yook, H.-E. Kim, Y.-H. Koh, Mater. Lett. 63 (17) (2009) 1545–1547, https://doi.org/10.1016/j.matlet.2009.04.012.
[23] F. Li, T. Jia, W. Dang, Z. Xu, K. Zhao, Y. Tang, Mater. Sci. Eng. A 820 (2021) 141584, https://doi.org/10.1016/j.msea.2021.141584.
[24] C. Chenglin,, Z. Jingchuan,, Y. Zhongda,, W. Shidong, Hydroxyapatite-Ti Functionally Graded Biomaterial Fabricated by Powder Metallurgy, Vol. 271, 1999.
[25] Y. Torres, J.J. Pavón, I. Nieto, J.A. Rodríguez, Metall. Mater. Trans. B 42 (4) (2011) 891–900, https://doi.org/10.1007/s11663-011-9521-6.
[26] X. Rao, C.L. Chu, Y.Y. Zheng, J. Mech. Behav. Biomed. Mater. 34 (2014) 27–36, https://doi.org/10.1016/j.jmbbm.2014.02.001.
[27] W. Xu, M. Chen, X. Lu, D. Zhang, H. Singh, Y. Jian-shu, Y. Pan, X. Qu, C. Liu, Corros. Sci. 168 (2020) 108557, https://doi.org/10.1016/j.corsci.2020.108557.
[28] J.E. de la Rosa, C. García-Cabezón, C. García-Hernández, E.J. Delgado-Pujol, F. J. García-García, A.R. Bocaccini, F. Martín-Pedrosa, Y. Torres, Appl. Surf. Sci. Adv. 26 (2025) 100723, https://doi.org/10.1016/j.apsadv.2025.100723.
[29] B. Li, Z. Li, X. Lu, Anti-Corros. Methods Mater. 59 (2) (2012) 57–62, https://doi.org/10.1108/00035591211210811.
[30] A.C. Vieira, A.R. Ribeiro, L.A. Rocha, J.P. Celis, Wear 261 (9) (2006) 994–1001, https://doi.org/10.1016/j.wear.2006.03.031.
[31] E. Kandaswamy, M. Harsha, V.M. Joshi, J. Trace Elem. Med Biol. (2024), https://doi.org/10.1016/j.jtemb.2024.127464.
[32] D.C. Rodrigues, P. Valderrama, T.G. Wilson, K. Palmer, A. Thomas, S. Sridhar, A. Adapalli, M. Burbano, C. Wadhwani, Materials 6 (11) (2013) 5258–5274, https://doi.org/10.3390/ma6115258.
[33] D.C. Rodrigues, R.M. Urban, J.J. Jacobs, J.L. Gilbert, J. Biomed. Mater. Res. B Appl. Biomater. 88 (1) (2009) 206–219, https://doi.org/10.1002/jbm.b.31171.
[34] J. Takadoum, Corrosion and Materials Degradation 4 (4) (2023) 644–658, https://doi.org/10.3390/cmd4040033.
[35] X. Gai, Y. Bai, J. Li, S. Li, W. Hou, Y. Hao, X. Zhang, R. Yang, R.D.K. Misra, Corros. Sci. 145 (2018) 80–89, https://doi.org/10.1016/j.corsci.2018.09.010.
[36] I.C. Lavos-Valereto, S. Wolynec, I. Ramires, A.C. Guastaldi, J. Mater. Sci. Mater. Med. 15 (2004) 55–59.
[37] A.K. Shukla, R. Balasubramaniam, S. Bhargava, Intermetallics (barking). 13 (6) (2005) 631–637, https://doi.org/10.1016/j.intermet.2004.10.001.
[38] S.L. de Assis, S. Wolynec, I. Costa, Electrochim. Acta 51 (8–9) (2006) 1815–1819, https://doi.org/10.1016/j.electacta.2005.02.121.
[39] I. Milošev, T. Kosec, H.-H. Strehblow, Electrochim. Acta 53 (9) (2008) 3547–3558, https://doi.org/10.1016/j.electacta.2007.12.041.
[40] V.A. Alves,, R.Q. Reis,, I.C.B. Santos,, D.G. Souza,, T. de F. Gonçalves,, M.A. Pereira-da-Silva,, A. Rossi,, L.A. da Silva, Corros. Sci. 51(10) (2009) 2473–82. 10.1016/j.corsci.2009.06.035.
[41] A.W.E. Hodgson, Y. Mueller, D. Forster, S. Virtanen, Electrochim. Acta 47 (12) (2002) 1913–1923, https://doi.org/10.1016/S0013-4686(02)00029-4.
[42] W. Lu, Y. Liu, X. Wu, X. Liu, J. Wang, Corros. Sci. 241 (2024) 112542, https://doi.org/10.1016/j.corsci.2024.112542.
[43] K. Domehri, M. Rajabi, M. Amirnejad, J. Mater. Eng. Perform. 34 (1) (2025) 857–869, https://doi.org/10.1007/s11665-023-09085-9.
[44] P.F. Ji, B. Li, B.H. Chen, F. Wang, W. Ma, X.Y. Zhang, M.Z. Ma, R.P. Liu, Corros. Sci. 170 (2020) 108696, https://doi.org/10.1016/j.corsci.2020.108696.
[45] J. Pan, D. Thierry, C. Leygraf, Electrochim. Acta 41 (7–8) (1996) 1143–1153, https://doi.org/10.1016/0013-4686(95)00465-3.
[46] A. Bordbar-Khiabani, M. Gasik, J. Mater. Res. Technol. 26 (2023) 356–370, https://doi.org/10.1016/j.jmrt.2023.07.113.
[47] S. Hu, T. Li, X. Li, G. Zhang, J. Li, F. Guo, D. Liu, J. Mater. Sci. 58 (2) (2023) 946–960, https://doi.org/10.1007/s10853-022-08128-1.
[48] D. Mareci, G. Ungureanu, D.M. Aelenei, J.C.M. Rosca, Mater. Corros. 58 (11) (2007) 848–856, https://doi.org/10.1002/maco.200704065.
[49] J.C.M. Souza, P. Ponthiaux, M. Henriques, R. Oliveira, W. Teughels, J.-P. Celis, L. A. Rocha, J. Dent. 41 (6) (2013) 528–534, https://doi.org/10.1016/j.jdent.2013.03.008.
[50] M. Liu, J. Li, D. Li, L. Zheng, Anti-Corros. Methods Mater. 68 (1) (2021) 9–16, https://doi.org/10.1108/ACMM-05-2020-2312.
[51] J. Lario, Á. Vicente Escuder, F. Segovia, V. Amigó, J. Mater. Res. Technol. 16 (2022) 1435–1444, https://doi.org/10.1016/j.jmrt.2021.12.085.
[52] S. Samuel, S. Nag, S. Nasrazadani, V. Ukirde, M. El Bouanani, A. Mohandas, K. Nguyen, R. Banerjee, J. Biomed. Mater. Res. A 94A (4) (2010) 1251–1256, https://doi.org/10.1002/jbm.a.32782.
[53] D.-I. Seo, J.-B. Lee, Npj Mater. Degrad. 7 (1) (2023) 44, https://doi.org/10.1038/s41529-023-00363-4.
[54] M. Shahsavari, A. Imani, R.F. Schaller, E. Asselin, J. Appl. Electrochem. 52 (6) (2022) 1003–1019, https://doi.org/10.1007/s10800-022-01683-0.
[55] I. El Ouarti, E.M. Lotfi, M. Ben Ali, A. Bouklouze, F. Abdallaoui, Odontology (2025), https://doi.org/10.1007/s10266-025-01136-y.
[56] M. Shahabi, A. Jahanbin,, H. Esmaily, H. Sharifi, S. Salari, J. Clin. Pedia. Dent. 35 (4) (2011) 429–32. 10.17796/jcpd.35.4.m17j2h5827861m55.
[57] S. Incerti Parenti, S. Guicciardi, C. Melandri, S. Sprio, E. Lafratta, A. Tampieri, G.A. Bonetti, Acta Odontol. Scand. 70(1) (2012) 49–55. 10.3109/00016357.2011.575083.
[58] M. Mikulewicz, P. Wołowiec, B.W. Loster, K. Chojnacka, J. Trace Elem. Med Biol. 31 (2015) 74–77, https://doi.org/10.1016/j.jtemb.2015.03.007.
[59] L.P. Faverani, V.A.R. Barão, G. Ramalho-Ferreira, M.B. Ferreira, I.R. Garcia-Júnior, W.G. Assunção, J. Biomed. Mater. Res. B Appl. Biomater. 102 (1) (2014) 22–30, https://doi.org/10.1002/jbm.b.32949.
[60] C. Abalos, A. Paul, A. Mendoza, E. Solano, C. Palazon, F.J. Gil, J. Mater. Eng. Perform. 22 (3) (2013) 759–766, https://doi.org/10.1007/s11665-012-0311-3.
[61] ASTM Standard F67-13, (2017).
[62] ASTM Standard F136-13, Specification for Wrought Titanium-6Aluminum-4Vanadium ELI (Extra Low Interstitial) Alloy for Surgical Implant Applications (UNS R56401), ASTM International, West Conshohocken, PA, 2013.
[63] L.D. Zardiackas, M.J. Kraay, H.L. Freese, Titanium, niobium, zirconium, and tantalum for medical and surgical applications, ASTM (2006).
[64] ASTM Standard E112-24, Standard Test Methods for Determining Average Grain Size, 2024.
[65] W.C. Oliver, G.M. Pharr, J. Mater. Res. 7 (6) (1992) 1564–1583, https://doi.org/10.1557/JMR.1992.1564/METRICS.
[66] W.C. Oliver, G.M. Pharr, J. Mater. Res. 19 (1) (2004) 3–20, https://doi.org/10.1557/jmr.2004.19.1.3.
[67] ASTM Standard E 384-22, Standard Test Method for Microindentation Hardness of Materials, ASTM: West Conshohocken,PA, USA, 2022.
[68] L.F. Nielsen, Mater. Struct. 31 (1998) 651–661.
[69] ASTM Standard G102-89, Standard Practice for Calculation of Corrosion Rates and Related Information from Electrochemical Measurements, 2015.
[70] Iso 23317, Implants for Surgery-in Vitro Evaluation for Apatite-Forming Ability of Implant Materials Implants, 2014.
[71] T. Kokubo, H. Takadama, Biomaterials 27 (15) (2006) 2907–2915, https://doi.org/10.1016/j.biomaterials.2006.01.017.
[72] K.H.W. Seah, R. Thampuran, S.H. Teoh, Corros. Sci. 40 (4–5) (1998) 547–556, https://doi.org/10.1016/S0010-938X(97)00152-2.
[73] F. Toptan, Turk. J. Chem. 44 (3) (2020) 805–816, https://doi.org/10.3906/kim-2001-40.
[74] V.V. Stolyarov, Y.T. Zhu, T.C. Lowe, R.K. Islamgaliev, R.Z. Valiev, Nanostruct. Mater. 11 (7) (1999) 947–954, https://doi.org/10.1016/S0965-9773(99)00384-0.
[75] R. Silva, J. Silva, C.C. Viana, C.R.M. Afonso, P. Hammer, D.C.C. Magalhães, A. H. Plaine, C.A.D. Rovere, J. Mater. Res. Technol. 35 (2025) 2055–2067, https://doi.org/10.1016/j.jmrt.2025.01.136.
[76] J. Li, Y. He, W. Shi, S. Xiang, W. Gao, Appl. Surf. Sci. 604 (2022) 154539, https://doi.org/10.1016/j.apsusc.2022.154539.
[77] P. Vlcak, J. Fojt, Z. Weiss, J. Kopeček, V. Perina, Surf. Coat. Technol. 358 (2019) 144–152, https://doi.org/10.1016/j.surfcoat.2018.11.004.
[78] C.E.B. Marino, L.H. Mascaro, J. Electroanal. Chem. 568 (1–2) (2004) 115–120, https://doi.org/10.1016/j.jelechem.2004.01.011.
[79] D. Mareci, R. Chelariu, I. Dan, D.M. Gordin, T. Gloriant, J. Mater. Sci. Mater. Med. 21 (11) (2010) 2907–2913, https://doi.org/10.1007/s10856-010-4147-9.
[80] P. Navarro, M. Barrera, A. Olmo, Y. Torres, J. Biomed. Mater. Res. A 113 (2025) 1, https://doi.org/10.1002/jbm.a.37797.
[81] J.C. Sánchez-López, V. Godinho, C. López-Santos, P. Navarro, L.M. Rodríguez-Albelo, M. Sánchez-Pérez, E. Jiménez-Piqué, Y. Torres, Appl. Surf. Sci. 680 (2025) 161366, https://doi.org/10.1016/j.apsusc.2024.161366.
[82] I.M. Makena, M.B. Shongwe, Int. J. Electrochem. Sci. 19 (3) (2024) 100495, https://doi.org/10.1016/j.ijoes.2024.100495.
[83] J. Fojt, L. Joska, Biomed. Mater. Eng. 23 (3) (2013) 183–195, https://doi.org/10.3233/bme-130743.
[84] I.M. Makena, M.B. Shongwe, G.T. Motsi, J. Bio Tribocorros. 11 (2025) 3, https://doi.org/10.1007/s40735-025-00989-8.
[85] A. Manoj, A.K. Kasar, P.L. Menezes, J. Bio Tribocorros. (2019), https://doi.org/10.1007/s40735-018-0194-4.
[86] B. Dabrowski, J. Kaminski, W. Swieszkowski, K.J. Kurzydlowski, Mater. Sci. Forum 674 (2011) 41–46, https://doi.org/10.4028/www.scientific.net/MSF.674.41.
[87] M. Braic, A. Vladescu, V. Braic, C.M. Cotrut, D. Stanciu, Mater. Corros. 66 (11) (2015) 1331–1337, https://doi.org/10.1002/maco.201508382.
[88] C. Vitelaru, N. Ghiban, A.C. Parau, M. Balaceanu, F. Miculescu, A. Vladescu, Materwiss. Werksttech. 45 (2) (2014) 91–98, https://doi.org/10.1002/mawe.201400191.
[89] M. Correa Rossi, B. Navarro Ventura, L. Milián, A.V. Escuder, V. Amigó Borrás, Metals (Basel) 12 (3) (2022), https://doi.org/10.3390/met12030476.
[90] A.K. Johansson, P. Lingström, D. Birkhed, Acta Odontol. Scand. 65 (6) (2007) 352–356, https://doi.org/10.1080/00016350701742372.
[91] E. Zhang, C. Zou, Acta Biomater. 5 (5) (2009) 1732–1741, https://doi.org/10.1016/j.actbio.2009.01.014.

[92] X. Liu, C. Ding, Z. Wang, Biomaterials 22 (14) (2001) 2007–2012, https://doi.org/10.1016/S0142-9612(00)00386-0.
[93] N. Taniguchi, S. Fujibayashi, M. Takemoto, K. Sasaki, B. Otsuki, T. Nakamura, T. Matsushita, T. Kokubo, S. Matsuda, Mater. Sci. Eng. C 59 (2016) 690–701, https://doi.org/10.1016/j.msec.2015.10.069.
[94] Q. Ran, W. Yang, Y. Hu, X. Shen, Y. Yu, Y. Xiang, K. Cai, J. Mech. Behav. Biomed. Mater. 84 (2018) 1–11, https://doi.org/10.1016/j.jmbbm.2018.04.010.
[95] G. Li, L. Wang, W. Pan, F. Yang, W. Jiang, X. Wu, X. Kong, K. Dai, Y. Hao, Sci. Rep. 6 (2016), https://doi.org/10.1038/srep34072.